GSFC JPSS CMO
April 15, 2014
Released

Joint Polar Satellite System (JPSS) Ground Project
Code 474
474-00048

Joint Polar Satellite System (JPSS) VIIRS Sea Surface Temperature Algorithm Theoretical Basis Document (ATBD)

For Public Release

Goddard Space Flight Center
Greenbelt, Maryland

National Aeronautics and
Space Administration

Joint Polar Satellite System (JPSS)
VIIRS Sea Surface Temperature
Algorithm Theoretical Basis Document (ATBD)

JPSS Electronic Signature Page

Prepared By:

Ray Godin
JPSS Data Products and Algorithms, EDR Lead
(Electronic Approvals available online at https://jpssmis.gsfc.nasa.gov/mainmenu_dsp.cfm

Approved By:

Eric Gottshall
JPSS Data Products and Algorithms Manager
(Electronic Approvals available online at https://jpssmis.gsfc.nasa.gov/mainmenu_dsp.cfm

Goddard Space Flight Center
Greenbelt, Maryland

Preface

This document is under JPSS Ground AERB configuration control. Once this document is approved, JPSS approved changes are handled in accordance with Class I and Class II change control requirements as described in the JPSS Configuration Management Procedures, and changes to this document shall be made by complete revision.

Any questions should be addressed to:

JPSS Ground Project Configuration Management Office
NASA/GSFC
Code 474
Greenbelt, MD 20771

Change History Log

Revision	Effective Date	Description of Changes (Reference the CCR & CCB/ERB Approve Date)
Original	04/22/2011	**474-CCR-11-0063:** This version baselines D43311, VIIRS Sea Surface Temperature Algorithm Theoretical Basis Document ATDB (ref Y2386), Rev C, dated 09/10/2010, as a JPSS document, version Rev –. This is the version that was approved for NPP launch. Per NPOESS CDFCB - External, Volume V – Metadata, doc number D34862-05, this has been approved for Public Release into CLASS. This CCR was approved by the JPSS Algorithm ERB on April 22, 2011.
A	08/21/2013	**474-CCR-13-1077 and 474-CCR-13-1137:** These CCRs were approved by the JPSS Algorithm ERB on August 21, 2013. Major modifications were made throughout the document.

Northrop Grumman Space & Mission Systems Corp.
Space Technology
One Space Park
Redondo Beach, CA 90278

Engineering & Manufacturing Development (EMD) Phase
Acquisition & Operations Contract

CAGE NO. 11982

VIIRS Sea Surface Temperature Algorithm Theoretical Basis Document ATBD (ref Y2386)

Document Date: 9/10/2010

Document Number: D43311
Revision: C

Point of Contact: Sid Jackson, Modeling & Simulations

ELECTRONIC APPROVAL SIGNATURES:

_____   _____

  Merit Shoucri, Modeling and Simulations Lead

Prepared by
Northrop Grumman Space Technology
One Space Park
Redondo Beach, CA 90278

Prepared for
Department of the Air Force
NPOESS Integrated Program Office
C/O SMC/CIK
2420 Vela Way, Suite 1467-A8
Los Angeles AFB, CA 90245-4659

Under
Contract No. F04701-02-C-0502

rthrop Grumman Space & Mission Systems Corp. **Space Technology** One Space Park Redondo Beach, CA 90278	NORTHROP GRUMMAN Raytheon

Revision/Change Record			**Document Number** D43311	
Revision	**Document Date**	**Revision/Change Description**		**Pages Affected**
---	01/17/2007	Initial PCIM Release to bring document into Matrix Accountability. Reference original document number: Y2386 delivered in 2002		All
A	08/08/2007	Revision A Release to bring document into Matrix Accountability. Contains revisions found in v5 r5 of the Raytheon document Y2386 delivered June 2005 as part of VIIRS 1.0.4 drop.		All (format and headers)
B	12/19/2008	Revision B. Updates ATBD to conform with changes in Sea Surface Temperature algorithm adopted by NPOESS to follow heritage algorithm		All
C	9/10/2010	Revision C: Updates ATBD in response to Document Convergence RFA 008 (ECR A-329)		9, 14, 27, 29

Revision/Change Record   **For Document No. Y2386**

Symbol	**Document Date**	**Authorization Date**	**Revision/Change Description**	**Pages Affected**
	03/2003	Sid Jackson	SPCR ALG00000007 NMD-EMD.03.591.009(assigned)	Title Page, Page i, vii, 1, 20-22, 28-39, 41-56, 64-81
	03/2003	Sid Jackson	SPCR ALG00000021 NMD-EMD.03.591.009(assigned)	Title Page, Page i, ii, xi, 10, 22, 28
	05/2005	Sid Jackson	SPCR ALG00000832 NMD-EMD.03.591.009(assigned)	Title Page, Page i-v, vii, xi, 1, 6, 7, 10, 11, 18-21, 27, 29, 39, 41, 43, 47, 49, 58, 59, 60, 61, 62
	06/2005	Sid Jackson	SPCR ALG00000854 NMD-EMD.03.591.009(assigned)	Title Page, Page i-vii, 1, 11, 20-22, 31, 32, 44, 48, 67, 68

TABLE OF CONTENTS

LIST OF FIGURES

LIST OF TABLES

GLOSSARY OF ACRONYMS

ACSPO	Advanced Clear-Sky Processor for Oceans
AOI	Angle of Incidence
AMI	Aerosol Model Index
AOT	Aerosol Optical Thickness
ATBD	Algorithm Theoretical Basis Document
ATSR	Along Track Scanning Radiometer
AVHRR	Advanced Very High Resolution Radiometer
BBR	Band-to-Band Registration
BT	Brightness Temperature
BTMn	VIIRS Emissive Band, where n = 12, 13, 14, 15, or 16
CAIV	Cost As an Independent Variable
CRTM	Community Radiative Transfer Model
DCS	Data Collection System
ECMWF	European Center for Medium-Range Weather Forecast
EDR	Environmental Data Record
EOS	Edge of Scan
GFS	Global Forecast System
GLI	Global Imager
GSD	Ground Sample Distance
HCS	Horizontal Cell Size
IDPS	Interface Data Processing Segment
IPO	Integrated Program Office
IR	Infrared
iQuam	In-situ SST Quality Monitor
JPSS	Joint Polar Satellite System
LOWTRAN	Low-resolution Transmission Model
LWIR	Longwave Infrared
MCSST	Multi-Channel Regression Method SST
MICROS	Monitoring of IR Clear-sky Radiances over Oceans for SST
MODIS	Moderate Resolution Imaging Spectroradiometer

MODTRAN	Moderate Resolution Transmission Model
MOSART	Moderate Spectral Atmospheric Radiance and Transmittance
MTF	Modulation Transfer Function
MWIR	Midwave Infrared
NCEP	National Centers for Environment Prediction
NEdT	Noise-Equivalent Temperature Difference
NESDIS	National Environmental Satellite, Data and Information Service
NODC	National Oceanographic Data Center
NPOESS	National Polar-orbiting Operational Environmental Satellite System
OSI-SAF	EUMETSAT Ocean and Sea Ice Satellite Application Facility
OCTS	Ocean Color and Temperature Scanner
P^3I	Pre-Planned Product Improvement
PW	Precipitable Water
QC	Quality Control
RMn	VIIRS Reflective Bands, where n = 5, 7, or 9
RMS	Root Mean Square
RTM	Radiative Transfer Model
RVS	Response Versus Scan Angle
SBRS	Santa Barbara Remote Sensing
SD	Standard Deviation
SRD	Sensor Requirements Document
SST	Sea Surface Temperature
SQUAM	SST Quality Monitor
TIR	Thermal Infrared
TOA	Top of Atmosphere
TPW	Total column Precipitable Water vapor content in the atmosphere
TRMM	Tropical Rainfall Measuring Mission
VIIRS	Visible Infrared Imager Radiometer Suite
VIRS	TRMM Visible Infrared Scanner
VZA	Satellite View Zenith Angle

ABSTRACT

This is the Algorithm Theoretical Basis Document (ATBD) for Sea Surface Temperature (SST) retrieval from Infrared (IR) radiance measured by the Joint Polar Satellite System (JPSS) Suomi National Polar-orbiting Partnership (S-NPP) Visible Infrared Imager Radiometer Suite (VIIRS), updated in May 2013, after approximately one and half year of the VIIRS performance on the orbit. SST is one of the VIIRS key global products and an input variable for other VIIRS products such as net heat flux. The SST Unit produces the VIIRS SST Environmental Data Record (EDR), for a skin SST (i.e. the temperature at the sea surface).

The initial SST algorithms for VIIRS have been developed by the NPOESS algorithm team prior to the S-NPP launch, based on the previous experience with AVHRR and MODIS instruments and using theoretical considerations. Several months after the launch, in May 2012, the coefficients for these algorithms have been recalculated at NOAA/NESDIS/STAR using matchups of VIIRS observations with *in situ* (drifters') SST. Although this update has improved the SST EDR performance to some extent, it remained suboptimal compared with another VIIRS SST product generated at NOAA with the Advanced Clear-Sky Processor for Oceans (ACSPO). Therefore, a comprehensive analysis of existing SST retrieval algorithms has been undertaken in order to find the optimal SST algorithm for VIIRS EDR. This study has shown that the performance of algorithms developed at the EUMETSAT Ocean and Sea Ice Satellite Application Facility is superior out of all other tested SST algorithms. These algorithms are the modifications of Non-Linear Split Window formulation using VIIRS Bands M15 (λ=10.8 µm) and M16 (λ=12.05 µm) for day and of Multichannel formulation, which also includes measurements from band M12 (λ=3.7 µm), for night. In order to improve accounting for atmospheric attenuation, these algorithms introduce dependencies of all regression coefficients on on satellite view zenith angle.

1.0   INTRODUCTION

1.1   PURPOSE

This document describes the theoretical basis of the SST algorithm, for retrieval of the VIIRS SST Environmental Data Record (EDR).   Algorithm validation, algorithm sensitivity, constraints, limitations, and assumptions are also discussed.

1.2   SCOPE

The SST algorithms described in this document will be used routinely to retrieve skin SSTs from VIIRS measurements. P^{3}I efforts may result in further enhancements to the current operational algorithms.

The next section provides a brief overview. Descriptions of the algorithm are presented in Section 3, along with discussions of algorithm sensitivity to various physical parameters. Calibration and validation are also discussed in Section 3. Constraints, assumptions, and limitations are identified in Section 4.

1.3   VIIRS DOCUMENTS

Reference to VIIRS documents is indicated by a number in italicized brackets, e.g., *[V-1]*.

1.4   REVISIONS

This is a major revision of the document and was made in response to a major change in the formulations of the default pre-launch SST algorithms for both daytime and nighttime measurements, based on analyses of VIIRS EDR SST performance during one and half a year of VIIRS functioning onboard the Suomi National Polar-orbiting Partnership satellite. The updated formulations of SST algorithms have been selected based on objective evaluation of existing SST retrieval algorithms, using an extended dataset of matchups of VIIRS observations and *in situ* SSTs. As a result, the algorithms developed at the EUMETSAT Ocean and Sea Ice Satellite Application Facility (OSI-SAF) and used for processing MetOp-A AVHRR data for a long time (OSI-SAF Low Earth Orbiter SST Product User Manual, 2009) have been selected. The daytime and nighttime algorithms represent modifications of the Non-Linear SST (NLSST) algorithm (Walton et al., 1998), and the Multichannel SST (MCSST) algorithm (McClain et al., 1983), respectively, with some additional terms emphasizing dependencies of regression coefficients on satellite view zenith angle. The daytime algorithm is also the fallback algorithm for night-time measurements.

2.0   EXPERIMENT OVERVIEW

2.1   OBJECTIVES OF SEA SURFACE TEMPERATURE RETRIEVALS

Most of the radiant energy arriving at the earth's surface is absorbed by the upper oceans. Some is released locally to the atmosphere, and some is stored for hours to days to seasons. The transport by the surface currents of heat that is subsequently released elsewhere is a major aspect of the climate system, and the poleward advection of heat in the ocean and atmosphere helps define the global climate system, and the response of the atmosphere to the heat released by the ocean determines some important characteristics of the weather. The sea-surface temperature (SST) is an indicator of the distribution of heat in the upper ocean, its patterns reveal the underlying surface currents, and it is a major determining factor in the exchange of heat, momentum and gases with the atmosphere. The ability of satellite-borne radiometers to provide measurements of SST in a self-consistent and accurate fashion on a global scale has resulted in satellite remote sensing having become one of the most important sources of SST data for a wide variety of applications.

The SST is a very variable quantity with a range of values from about -1.9^{o}C (the freezing point of sea water) to greater than 30°C, with spatial gradients in excess of 1 K km^{-1} possible at surface frontal outcrops. The magnitude of temporal variations of SST around the seasons is often only several degrees, but similar changes can be experienced in the course of a day (e.g. Minnett, 2003; Gentemann et al., 2003; Stuart-Menteth et al., 2003; Gentemann and Minnett, 2008; Gentemann et al., 2008b). A well-known SST perturbation that influences the global-scale weather patterns is the El Niño, in which the SST over the eastern equatorial Pacific may be 4-5 K higher than in the normal situation. SST is also a good indicator of global warming (Good et al., 2007), and for this application, decadal-length time series have to be constructed (Kilpatrick et al., 2001). The characteristics of the SST fields determine the requirements placed on the design, construction and calibration of the satellite radiometers.

The accuracy of infrared SST determination from satellite depends on how well the effects of the intervening, cloud-free atmosphere are corrected. Water vapor is the main contributor to the atmospheric effect in the infrared, and it is very variable in both space and time. This variability requires that for a correction to be effective it has to be applied on a pixel-by-pixel basis. Other gases are relatively well mixed and less problematic in their correction.   The accuracy has improved significantly since the development of radiometers with two or more atmospheric window channels within MWIR and LWIR transmission windows (e.g., McClain et al., 1983; Kilpatrick et al., 2001).   The fundamental basis of multi-channel SST algorithms is the differential water vapor absorption in the various atmospheric window regions of the spectrum (McMillin, 1975).

The majority of existing SST algorithms retrieves SST from observed brightness temperatures (BT, T_B) via regression, using modifications of two approaches developed earlier for AVHRR. The "Multichannel" SST (MCSST) approach [*McClain et al.,* 1985] is customarily used with three bands centered at 3.7, 11 and 12 μm, and at night only, thus avoiding contamination of 3.7 μm band with reflected solar radiance. The "Nonlinear" SST (NLSST) approach [*Walton et al*., 1998] exploits two split-window bands centered at 11 and 12 μm and *a priori* SST T_S^0 which is

2

used as a proxy for atmospheric humidity. Although the NLSST is mostly used during daytime, it can be also used at night, in conjunction with using the more transparent 3.7 μm band. The derivation of regression algorithms combines satellite and *in situ* measurements.

A common problem of regression SST algorithms is that SST accuracy and precision are sensitive to the atmospheric attenuation and such its proxies as view zenith angle and water vapor content in the atmosphere. As a result, SST accuracy and precision significantly vary in space. As alternatives to regression, several SST algorithms based on a radiative transfer model (RTM) have been recently developed (Merchant et al, 2008; Le Borgne et al., 2011; Petrenko et al., 2011). These algorithms have been shown capable of providing more uniform SST accuracy and precision than it is possible with pure regression. However, since the JPSS Interface Data Processing Segment (IDPS) currently does not support on-line RTM simulations, the RTM-based algorithms cannot be implemented for EDR SST. Therefore, the effort has been made to select for IDPS the regression SST algorithm with the most appropriate combination of retrieval characteristics.

The radiant energy leaving the ocean surface is emitted by a very thin (<1mm) layer, often referred to as the skin layer, and its temperature is called the skin temperature. At the air-sea interface, the ocean is warmer than the overlying atmospheric layer, and thus heat flows from the ocean to the atmosphere. Close to the interface, the heat flow is by molecular conduction, and this requires a vertical temperature gradient. As a consequence, the skin temperature is cooler than that of the water below by a variable amount, up to ~0.5K. The relationship between skin and bulk SSTs has been investigated by a number of scientists (e. g., Schluessel *et al.*, 1990; Donlon et al., 2002; Wick et al., 2002). If surface wind speed, w, is available, then the following relationship between skin and bulk SST was proposed by Donlon et al (2002):

$$\text{SST}_{bulk} = \text{SST}_{skin} - [0.14 + 0.30\exp(-w/3.7)]$$

During daytime, the relationship between skin and bulk SSTs is more complex, due to the effect of the diurnal thermocline. Its modeling requires knowledge of fluxes at the surface, including their history. In this ATBD, the coefficients for regression SST algorithm are calculated from matchups of BTs and *in situ* bulk SSTs. On the other hand, the observed BTs, from which the SST products are derived, are sensitive to skin SST. As a result, retrieved SST reflects variations in skin SST, but its average value is anchored to bulk SST. Recently, Castro et al. (2010) have found that the accuracy of regression, produced from matchups of bulk SST and AVHRR BTs, is not worse (and often is better) than the accuracy of regression, produced from matchups of skin SST and AVHRR BTs. Establishing of a global and reliable relationship between skin and bulk SST is still a subject of the future studies..

The VIIRS SST EDR developed prior to S-NPP VIIRS launch, included both skin and bulk SST, with skin SST being biased with respect to bulk SST by a constant offset of -0.17 K. The new version of VIIRS SST EDR, updated in May 2013, includes only skin SST, and bulk SST layer is replaced with first guess (a priori) SST, produced from L4 analysis SST field (e.g., NCEP GFS). Users interested in bulk SST can easily produce it from skin SST by adding to skin SST 0.17 K.

2.2   INSTRUMENT CHARACTERISTICS

The VIIRS MWIR and LWIR bands must be positioned to optimize their use for SST determination. Bands in the LWIR atmospheric transmission window are also located near the maximum intensity in Planck's function at temperatures characteristic of the sea surface. Influences of ozone and other variable atmospheric absorbers are best avoided. There are two suitable regions for LWIR band selection: 8-9 μm and 10-13 μm. Three VIIRS LWIR bands are located in these two regions. Figures 1 and 2 show the radiance at the height of the satellite and the atmospheric transmission for the Thermal IR (TIR) spectrum simulated using the MODTRAN atmospheric radiative transfer code and five standard atmospheres. Bands in the MWIR are located where the atmosphere is transparent and less variable. Figure 2 shows that the 3.4-4.2 μm region is a suitable atmospheric window. Two VIIRS MWIR bands are located in this window. The requirement to produce SSTs consistent with those from heritage sensors is also one of the factors for VIIRS band selection. Table 1 shows the bands used to retrieve SST from measurements of existing infrared satellite radiometers. In earlier versions of this ATBD, we investigated the effects of band location in the MWIR and LWIR windows.   Those documents summarize the flowdown of the SRD requirements for the VIIRS SST to the present VIIRS IR band selection.

To meet the VIIRS SST measurement requirements, the sensor must have very low radiometric noise in the IR bands. Knowledge of the characteristics of the infrared bands is very important. The detailed specification of the current version of the sensor design is listed in Table 2.
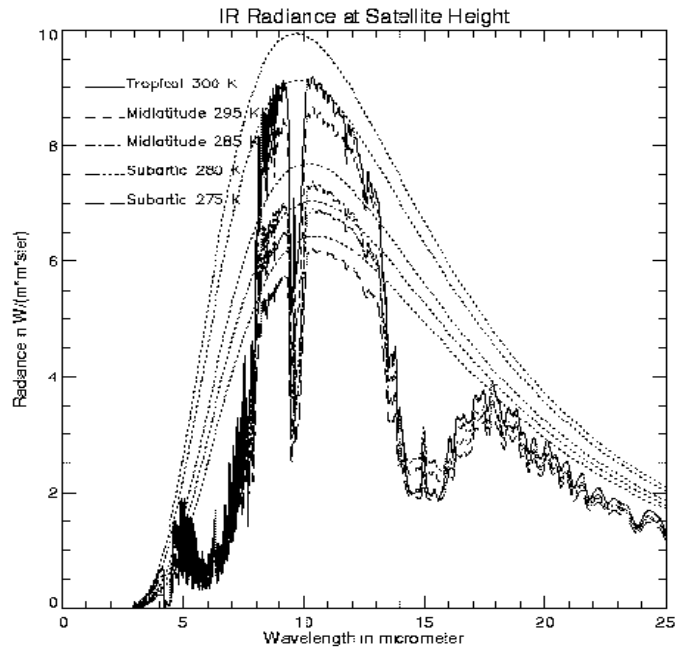
Figure 1. IR radiance at satellite height for five standard atmospheres simulated by MODTRAN. The SST at the base of the atmospheres is given in the key in the figure.
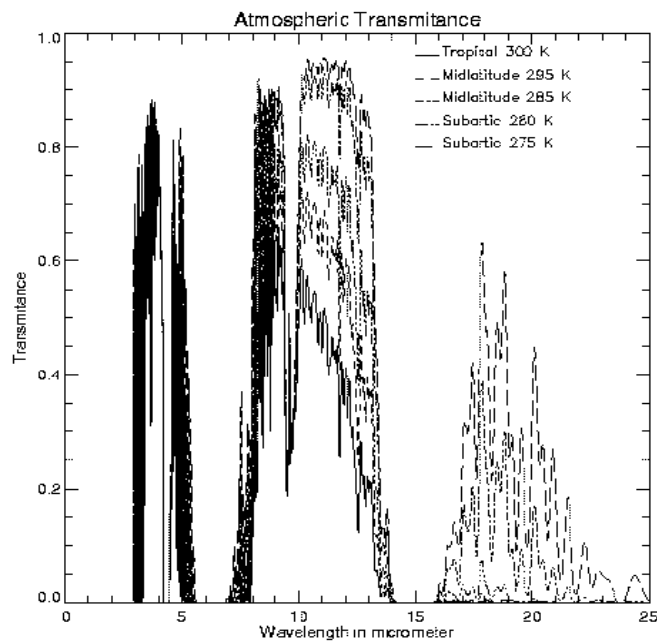
Figure 2. As Figure 1, but showing atmospheric transmittance.

Table 1. Channel Characteristics of Satellite-borne IR Radiometers

VIIRS baseline		MODIS		AVHRR		(A)ATSR	
$\lambda\mu m$	NEΔT K	$\lambda\mu m$	NEΔT K	$\lambda\mu m$	NEΔT K	$\lambda\mu m$	NEΔT K
3.7	0.065	3.75	0.05	3.75	0.12	3.7	0.019
4.0	0.078	3.96	0.07				
		4.02	0.07				
10.8	0.038	11.03	0.05	10.5	0.12	10.8	0.028
12.0	0.070	12.02	0.05	11.5	0.12	12.0	0.025

To meet the VIIRS SST measurement requirements, the sensor must ensure very low radiometric noise for IR bands, especially the 10-12 μm window. Well-placed windows in the 3.6-4.2 μm are also important. The detailed specification of the current version of the sensor design is listed in Table 2.

Table 2. Sensor Performance for Sea Surface Temperature

Wave-length μm	Band Widthμm	Native Sensor				Ttyp K	NEΔT K	Nadir						Effective Algorithm NEΔT K
		GSD						Onboard Aggregation Factor		On ground Aggregation Factor		Effective Algorithm GSD m		
		Nadir m		EOS m										
		Trk	Scn	Trk	Scn			Trk	Scn	Trk	Scn	Trk	Scn	
3.7	0.180	742	262	1094	617	300	0.065	1	3	1	1	742	786	0.038
4.0	0.155	742	262	1094	617	300	0.078	1	3	1	1	742	786	0.045
10.8	1.000	742	262	1094	617	300	0.038	1	3	1	1	742	786	0.022
12.0	0.950	742	262	1094	617	300	0.070	1	3	1	1	742	786	0.040

2.3   SST RETRIEVAL STRATEGY

The following operations are applied to produce the SST:

- A land/ocean mask is used to identify the ocean pixels to process.
- A cloud cover mask and a snow/ice mask are used to eliminate cloud-contaminated or snow/ice-covered pixels. The SST algorithms are not run under confident-cloudy sky conditions; all other cloud conditions the SST is derived, but the results are flagged for quality assurance.

- Satellite zenith angle is read in from the moderate resolution geolocation product.
- A day / night flag based on the solar zenith is to determine whether day or night retrieval is appropriate.
- Calibrated brightness temperatures are read in from the sensor data record (SDR). Coefficients are loaded for skin SST retrievals.
- Skin SST is calculated using regression equations from the split window algorithm during the day, and from the triple-window algorithm at night; the nighttime fallback algorithm is the split window formulation.

3.0 ALGORITHM DESCRIPTION

3.1 PROCESSING OUTLINE

Figure 3 depicts the processing concept for SST retrieval.

Figure 3. SST High Level Flowchart: Statistical Method.

3.2   ALGORITHM INPUT

3.2.1 VIIRS Data

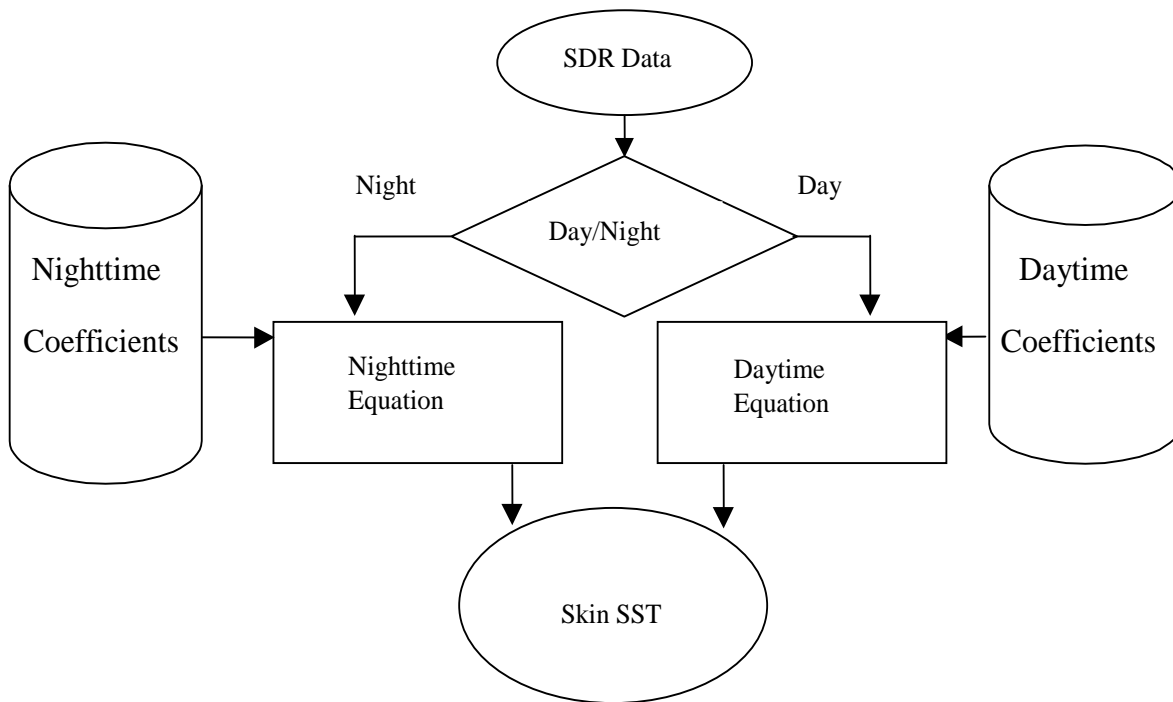Required inputs necessary for the SST retrieval from the VIIRS data stream are cloud mask, snow/ice mask, and TOA brightness temperatures (3.7, 10.76, and 12.05 μm).

3.2.2   Non-VIIRS Data

Non-VIIRS ancillary data includes land/ocean mask.

3.3   THEORETICAL DESCRIPTION OF SST RETRIEVAL

3.3.1   Physics of the Problem

In clear sky conditions, the outgoing IR spectral radiance at the top of atmosphere can be represented by:

$$L(\lambda,\mu) = \tau(\lambda,\mu)\varepsilon(\lambda,\mu)B(\lambda,T_s) + L_a(\lambda,\mu) + L_s(\lambda,\mu,\mu_0,\varphi_0)$$
$$+ \tau(\lambda,\mu)(1-\varepsilon(\lambda,\mu))L_d(\lambda,\mu,\mu_0,\varphi_0) + \tau(\lambda,\mu)L_r(\lambda,\mu,\mu_0,\varphi_0) \tag{1}$$

where τ is the transmissivity, ε the surface spectral emissivity, B the Planck function, L_a the upwelling, thermal path radiance, L_s the path radiance resulting from scattering of solar radiation. L_d is the solar radiance at the surface and L_r the solar diffuse radiation and atmospheric thermal radiation reflected by the surface. $\mu = \cos(\theta)$, $\mu_0 = \cos(\psi)$, where θ is the satellite zenith angle, ψ the solar zenith angle. φ_0 is the azimuth angle between the sun and the satellite.

λ is the center wavelength of a narrow spectral interval, defined by the relative spectral response function for each band and detector. Equation 1 is applicable in the 3-14 μm range. The complete simulation of atmospheric radiative transfer is necessary to determine the values of all terms on the right side. This equation has been used in many atmospheric radiation models including LOWTRAN (Kneizys et al., 1988), MODTRAN (Berk et al., 1989), RADGEN (Závody et al., 1995) and MOSART (Cornette et al., 1994). The inversion of Equation 1 is not straightforward if the atmospheric conditions are unknown.

To facilitate the accurate derivation of SST, we should use window bands with no or little atmospheric effect on the propagation of the infrared radiation. As shown in Figures 1 and 2 the wavelength intervals between 3.5–4.2 μm, 8–9 μm, and 10–13 μm are atmospheric transmission windows. For a perfect window, the total atmospheric transmittance $\tau(\lambda \ \mu)$ would be 1.0. However, as indicated in Figure 2, the transmittances at these windows are <1.0 and are functions of the atmospheric state. The main absorber for these windows is atmospheric water vapor.

The effect of water vapor in the transmissivity of the different spectral windows is illustrated in Figure 4 (Sobrino et al., 2003). The water vapor effects are much more pronounced in the thermal infrared window, with the mid-infrared transmission window being much less sensitive

9

to variations in the water vapor. Figure 4 is based on MODTRAN simulations using atmospheric states derived from radiosondes in the TIGR (TOVS Initial Guess Retrieval data base) (Chesters et al., 1983).
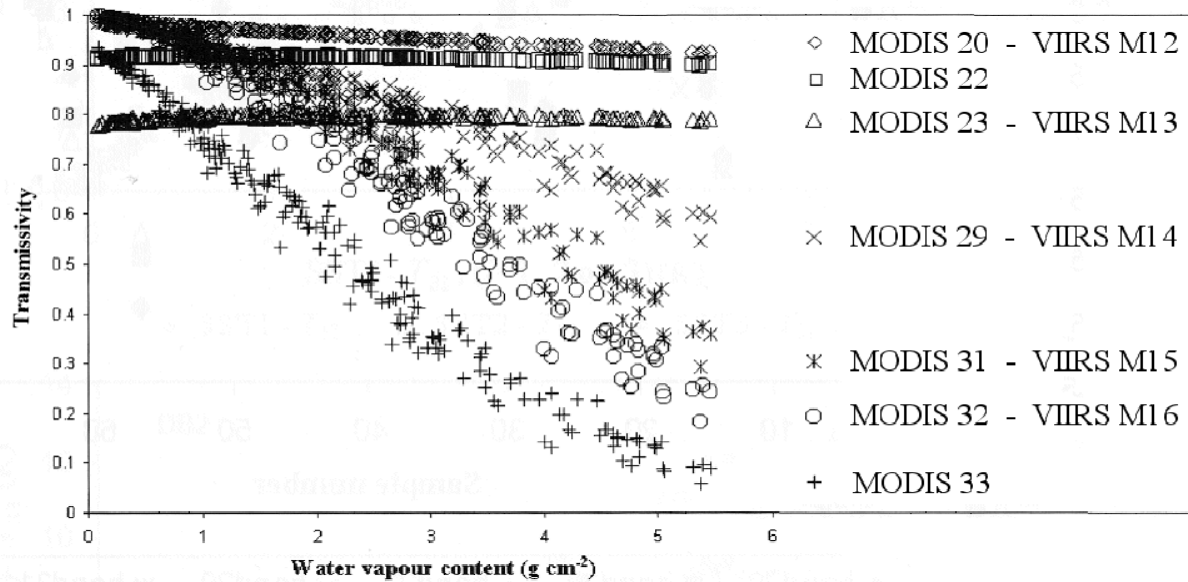
Figure 4. The relationships between atmospheric transmissivity and atmospheric water vapor content (after Sobrino et al., 2003). The data points were derived by radiative transfer modeling using a large data base of atmospheric profiles and the relative spectral response functions of the MODIS on *Terra*. The MODIS bands, and the corresponding VIIRS bands, are shown in the key at the right.

The saturation water vapor concentration is governed by the Clausius-Clapeyron equation which indicates that the saturation vapor pressure of a gas varies approximately exponentially with absolute temperature. Given the close thermodynamic coupling between the ocean and atmosphere, it is expected that a clear relationship exists between the atmospheric water vapor content and the SST. This has been demonstrated with satellite microwave radiometric measurements (e.g. Stephens, 1990) which reveal a non-linear increase in integrated water vapor content (precipitable water) with SST (Figure 5).

The consequence of the relationships between SST and atmospheric water vapor, and between water vapor and spectrally dependent atmospheric transmissivity, lead to a non-linear dependence of the brightness temperatures, measured at orbital height in the different spectral bands of infrared radiometers, on the SST. This is illustrated in Figure 6 which shows simulated brightness temperature deficits (the difference in the brightness temperature and the SST) in selected MODIS bands that correspond to VIIRS bands, as functions of SST. The use of MODIS relative spectral response functions in these simulations in place of those from VIIRS will introduce small discrepancies, but serve to illustrate the nature of the interaction between the cloud-free atmosphere and the infrared radiation.
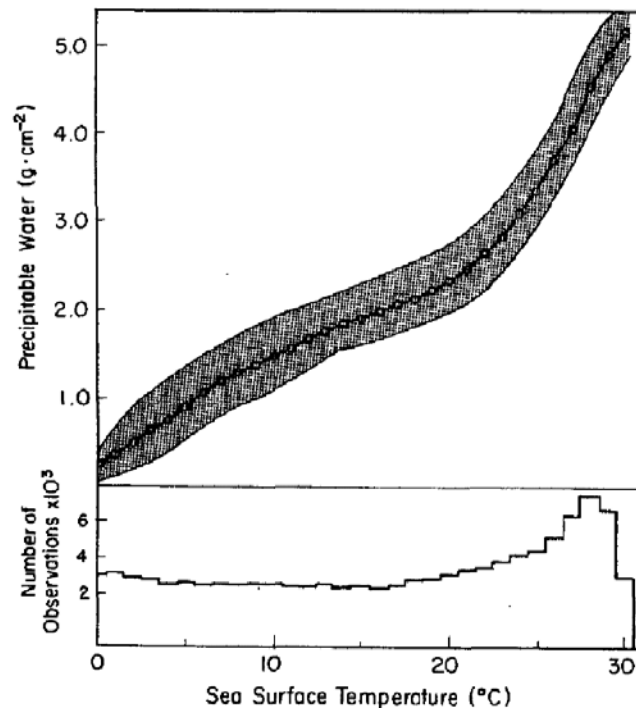
Figure 5. The relationship between annually averaged vertically integrated atmospheric water vapor content (precipitable water) and the SST (top), and the histogram, of the global SST values (bottom). The data were derived from measurements of the Scanning Multichannel Microwave Radiometer (SMMR) on the Nimbus-7 satellite. (From Stephens, 1990)

The representation of the cloud-free atmospheric variability for the radiative transfer code was provided by a set of atmospheric profiles, 2790 in number, from a data assimilation model used in weather prediction. These were derived from the output of the ECMWF (European Centre for Medium-range Weather Forecasting) data assimilation model at 10° latitude-longitude resolution over the oceans for 12 realizations through 1996. This has the advantage of near-uniform coverage over the oceans and good sampling in time.

The atmospheric radiative transfer model used to derive the results shown in Figure 6 is the line-by-line spectral code developed for the algorithm derivation for the ATSR (Závody et al., 1995), adapted to accommodate the latest version of the water-vapor continuum spectrum (Clough et al., 1989, subsequently revised by Han et al., 1997 and discussed in Merchant et al., 1999), with improved spectral parameters for atmospheric components from the AFGL data base This radiative transfer model is also the basis of the atmospheric correction algorithm applied to the measurements of the Along Track Scanning Radiometer (ATSR) series on the European satellites ERS-1, ERS-2 and Envisat. Again, the SST retrievals have been validated using independent measurements (Mutlow et al., 1994; Smith et al., 1994; Noyes et al., 2006). For the MODIS simulations, the model spectral ranges were 3.5 to 4.2μm and 6.2 to 14.7μm, with a spectral resolution of 0.04 cm^{-1}.

The output of the radiative transfer model comprises three sets of spectra for each atmospheric profile. These are of the upwelling atmospheric emission at the top of the atmosphere ($L_{atm}\uparrow(\theta,\lambda)$), downwelling atmospheric emission at the bottom of the atmosphere ($L_{atm}\downarrow(\theta,\lambda)$), and of the atmospheric transmission ($\tau(\theta,\lambda)$), where θ is the propagation angle relative to vertical. The spectrum of the total infrared radiance at the top of the atmosphere ($L\uparrow(\theta,\lambda)$) is derived by:

$$L\uparrow(\theta,\lambda) = L_{atm}\uparrow(\theta,\lambda) + ((1-\epsilon(\theta,\lambda)) * L_{atm}\downarrow(\theta,\lambda) + \epsilon(\theta,\lambda)*B(skinSST, \lambda))* \tau(\theta,\lambda) \qquad (2)$$

where $\epsilon(\theta,\lambda)$ is the emissivity of the sea-surface at wavelength λ and emission angle θ, and B is Planck's function at the temperature of the skin of the ocean, determined for each profile as an imposed air-sea temperature difference. The propagation of the infrared radiation through the atmosphere can be considered as a collimated beam at a given zenith angle because at infrared wavelengths the atmosphere can be considered to be non-scattering. The emission angle equals the satellite zenith angle.

The surface emissivity enters in two places: in the emission of the sea surface and in the reflection of $L_{atm}\downarrow(\theta,\lambda)$ as, through Kirchhoff's Law, the reflectivity is (1- $\epsilon(\theta,\lambda)$). The values used in these simulations were taken from the modeled results of Watts et al., 1996) which includes a specific wind-speed dependence. Subsequent research has shown that the wind speed dependence of $\epsilon(\theta,\lambda)$ has been over-emphasized in a number of well-used models results (e.g. Masuda et al., 1988, and Wu and Smith, 1997) as well as Watts et al., 1996) when compared to hyperspectral measurements at sea (Hanafin and Minnett, 2005; Nalli et al., 2008a) and more rigorous modeling (Nalli et al., 2008b). Thus, the consequences of the use of a single emissivity, neglecting wind speed effects, for each emission angle are of little consequence in these simulations.

Simulations were done for a range of satellite zenith angles (θ) and air-sea temperature differences (i.e. a skin SST was specified at the base of each atmosphere through a range of air-sea temperature differences: -3, -2, -1, 0 1 K). The behavior of the temperature deficits in *Terra* MODIS Bands 20, 23, 31 and 32 are shown in Figure 6. Figure 6a is for a satellite zenith angle of 0° (i.e. at nadir, at the sub-satellite track at the center of the swath) and Figure 6b at a satellite zenith angle of 55°, towards the edges of the swath. The points in each scatter diagram occur in groups of five representing the five different air-sea temperature differences at the base of each representation of the atmosphere. The magnitudes of the temperature deficits increase with satellite zenith angle, resulting from the effects of the increased atmospheric path length and decreasing surface emissivity. For bands 31 and 32 in the thermal infrared there are two distinct regimes with different sensitivities of the temperature deficits to the SST. This is caused primarily by the increasing atmospheric water vapor burden, which is highly correlated with the SST (Stephens, 1990), and which contributes a larger proportion of the spectral radiance measured in space in tropical conditions (Figure 5) than in higher latitudes.

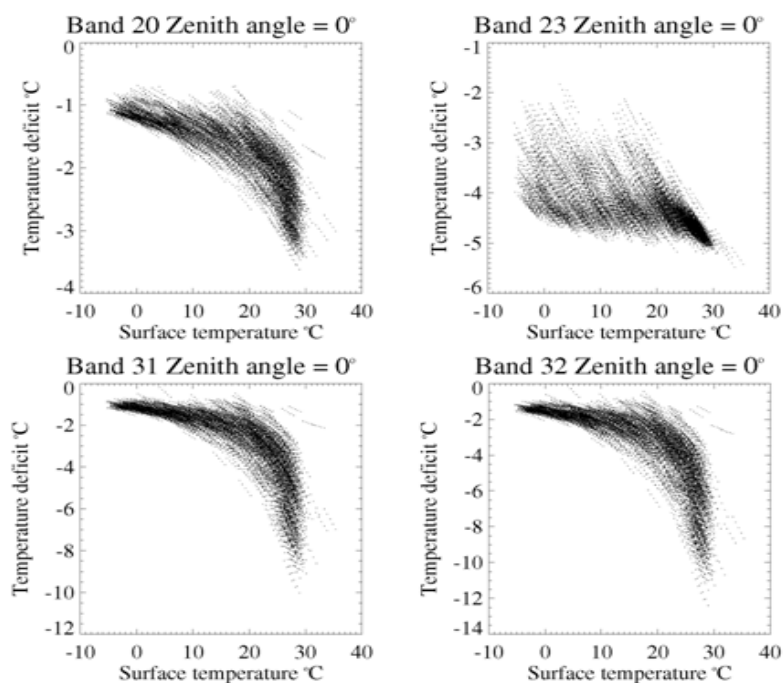**Figure 6. Simulated brightness temperature deficit for the MODIS bands corresponding to the VIIRS bands to be used for SST derivation. These simulations are expected to approximate very well the characteristics of the VIIRS measurements. The values here are for nadir measurement, at the center of the swath, at a zenith angle of 0°.**
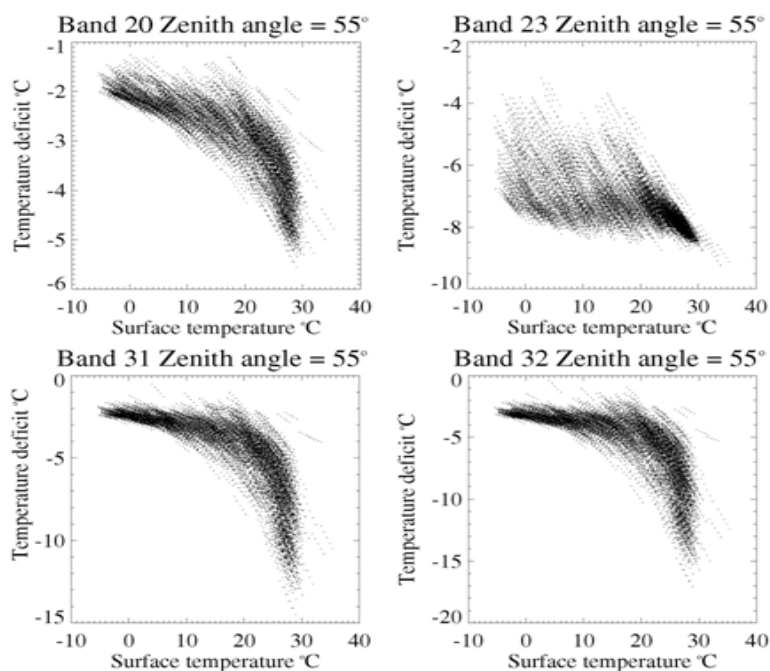

Figure 7. As Figure 6, but for a satellite zenith angle of 55°.

3.3.2 Mathematical Description of the SST Algorithms

3.3.2.1. The pre-launch SST algorithm

The initial daytime SST algorithm, implemented in the IDPS system during preparations to the S-NPP VIIRS mission and used for processing observations from VIIRS after its launch, is a modification of the Pathfinder algorithm developed by the University of Miami and used to process AVHRR data at NOAA/NESDIS/NODC (Kilpatrick et al., 2001). The daytime equation is as follows:

$$T_S = b_0 + b_1 T_{B11} + b_2 \Delta T_{11-12} T_S^0 + b_3 \Delta T_{11-12} S_\theta \tag{4a}$$

Here, T_S is retrieved SST; T_{B11} and T_{B12} are BTs at 11 μm and 12 μm, respectively; T_S^0 is first guess SST (in degrees Kelvin), obtained from the analysis (L4) SST field. $\Delta T_{11-12} = T_{B11} - T_{B12}$; $S_\theta = sec(\theta) - 1$; and a_i ($i=0,…,5$) and b_i ($i=0,…,3$) are regression coefficients. The equation (4a) is used with two separate sets of coefficients for conditions of "low" and "high" atmospheric humidity. The humidity conditions are identified by the value of ΔT_{11-12}:

$$T_S = T_S^L, \text{ if } \Delta T_{11-12} < \Delta T_{11-12}^L; \tag{4b}$$

$$T_S = T_S^H, \text{ if } \Delta T_{11-12} > \Delta T_{11-12}^H; \tag{4c}$$

$$T_S^L = a_0^L + a_1^L T_{B11} + a_2^L \Delta T_{11-12} (T_S^0 + X) + a_3^L \Delta T_{11-12} S_\theta \tag{4d}$$

$$T_S^H = a_0^H + a_1^H T_{B11} + a_2^H \Delta T_{11-12} (T_S^0 + X) + a_3^H \Delta T_{11-12} S_\theta, \tag{4e}$$

For intermediate ΔT_{11-12} values, $\Delta T_{11-12}^L \leq \Delta T_{11-12} \leq \Delta T_{11-12}^H$, T_S is found by interpolation:

$$T_S = T_S^L + (T_S^H - T_S^L)(\Delta T_{11-12} - \Delta T_{11-12}^L)/(\Delta T_{11-12}^H - \Delta T_{11-12}^L), \tag{4f}$$

Here, $\Delta T_{11-12}^L = 0.5K$, $\Delta T_{11-12}^H = 0.9K$. Regression coefficients for low humidity conditions, a_i^L, $i=0,…,3$, are derived from the part of matchups, for which $\Delta T_{11-12} < (\Delta T_{11-12}^H + \Delta T_{11-12}^L)/2$; and the coefficients for high humidity conditions, a_i^H, $i=0,…,3$, are derived from matchups, for which $\Delta T_{11-12} > (\Delta T_{11-12}^H + \Delta T_{11-12}^L)/2$.

The nighttime equation takes the following form:

$$T_S = b_0 + b_1 T_{B11} + b_2 \Delta T_{11-12} T_S^0 + b_3 \Delta T_{11-12} S_\theta \tag{5}$$

Here, $\Delta T_{3.7-12} = T_{B3.7} - T_{B12}$ is BT at 3.7 μm.

The monitoring of VIIRS SST retrievals performed on a daily basis during more than a year-long time period since 21 January 2012, in the NOAA SST Quality Monitor (SQUAM, *Dash et al.*, 2010, available at www.star.nesdis.noaa.gov/sod/sst/squam/, see also Section 3.6.2) and in the Monitoring of IR Clear-sky radiances over Oceans for SST (MICROS; *Liang and Ignatov*, 2011, 2013, available at www.star.nesdis.noaa.gov/sod/sst/micros/), has shown that the performance of the initial VIIRS EDR SST algorithm is suboptimal, particularly compared with the SST

produced by another processing system, operated by NOAA, the Advanced Clear-Sky Processor for Oceans (ACSPO).

3.3.2.2. The ACSPO Algorithms.

Although the ACSPO SST algorithms are not suggested for implementation within IDPS, the ACSPO SST product has been used as a benchmark for evaluation of the IDPS EDR SST performance, as discussed in Section 3.6.2. Therefore, here we provide a brief description of the ACSPO algorithms. ACSPO is a processing system developed at NOAA/STAR. Since May 2008, ACSPO has been used for operational processing the Advanced Very High Resolution Radiometer (AVHRR) data at the NOAA Office of Satellite and Product Operations (OSPO). The newer ACSPO versions are being continuously developed and used at STAR for experimental processing of data from all AVHRR, Moderate Resolution Imaging Spectroradiometer (MODIS) and VIIRS sensors [*Ignatov et al.*, 2012; *Liang and Ignatov*, 2013]. As of this writing, ACSPO employs heritage regression SST equations as they were implemented in the Main Unit Task system [*Ignatov et al.*, 2004], but the coefficients of regression equations were recalculated to accommodate the new ACSPO clear-sky mask (Petrenko et al., 2010), and to extend retrievals to full sensors' swaths. At night (i.e., when solar zenith angle, SZA > 90°), the ACSPO uses an MCSST equation in the following form:

$$T_S = a_0 + a_1 T_{B11} + a_2 T_{B3.7} + a_3 T_{B12} + a_4 \, \Delta T_{3.7\text{-}12} \, S_\theta + a_5 S_\theta \qquad (6)$$

The daytime ACSPO equation is of NLSST type:

$$T_S = b_0 + b_1 T_{B11} + b_2 \Delta T_{11\text{-}12} \, (T_S^{\,0} - 273.15) + b_3 \, \Delta T_{11\text{-}12} \, S_\theta \qquad (7)$$

As of this writing, the ACSPO equations are derived from matchups without "bulk/skin" correction. Therefore, ACSPO SST represents "bulk" SST.

3.3.2.3. The SST algorithm selected for IDPS SST EDR.

Due to suboptimal performance of the prelaunch versions of VIIRS EDR SST algorithms, the evaluation of the operational SST algorithms used at different processing centers, as well as some newly proposed approaches was undertaken in order to select more efficient SST algorithms for VIIRS (Petrenko et al., 2013). The analysis was based on dataset of matchups (MDS) of VIIRS brightness temperatures and quality *in situ* SST collected with the *in situ* Quality Monitor (*i*Quam; *Xu and Ignatov*, [2010], available at www.star.nesdis.noaa.gov/sod/sst/iquam/) from 15 April 2012 to 14 April 2013. As a result of these analyses, the algorithms developed at the EUMETSAT Ocean & Sea Ice Satellite Application Facility (OSI-SAF) have shown to be superior. The main difference between the OSI-SAF algorithms (Brisson et al., 2002; OSI-SAF Low Earth Orbiter SST Product User Manual, 2009) and the pre-launch IDPS algorithms is that the OSI-SAF algorithms emphasize the dependencies of regression coefficients on satellite view zenith angle rather than stratify the coefficients in terms of proxies of the atmospheric humidity. The formulations of the OSI-SAF equations specifically for VIIRS have been suggested by *Lavanant et al*. (2012).

The daytime equation is the analogue of (4a), in which the coefficients at all regressors are the functions of S_θ and T_s^0 is substituted in degrees Celsius rather than Kelvin:

$$T_S = b_0 + (b_1 + b_2 S_\theta) T_{11} + [b_3 + b_4 (T_s^0 - 273.15) + b_5 S_\theta] \Delta T_{11-12} + b_6 S_\theta, \qquad (8)$$

The algorithm (8) does not use any further stratification of regression coefficients. The dependencies of coefficients on S_θ are also introduced in the nighttime OSI-SAF equation:

$$T_S = a_0 + (a_1 + a_2 S_\theta) T_{3.7} + (a_3 + a_4 S_\theta) \Delta T_{11-12} + a_5 S_\theta \qquad (9)$$

The important difference between the nighttime equations (5) and (9) is that (9) includes $T_{3.7}$ as a separate regressor. This increases the sensitivity of T_s to true SST, due to higher transparency of the band at 3.7 μm and higher than in the band 11 μm sensitivity of $T_{3.7}$ to SST.

The coefficients for equations (8) and (9) were calculated from the MDS collected from 15 April 2012 to 14 April 2013. Since the drifters measure "bulk" SST, the initial regression equations were also adjusted to "bulk" SST. In order to produce "skin" SST, a constant bias of 0.17 K was subtracted from the offsets $b0$ in (8) and $a0$ in (9). The coefficients for "skin" SST are presented in Tables 3 and 4. Table 3 also presents the nighttime coefficients for equation (8), which is used as a fallback equation.

Table 3. Daytime and nighttime coefficients for the equation (8)

	b_0	b_1	b_2	$b3$	b_4	b_5	b_6
Day	3.885431	0.991024	0.0199173	0.450966	0.0666661	0.669463	-4.66451
Night	6.01363	.983461	0.0237138	0.408630	0.0698974	0.575228	-5.53460

Table 4. Coefficients for the nighttime equation (9)

a_0	a_1	a_2	$a3$	a_4	a_5
-1.22636	1.00787	0.0314639	0.934653	0.255025	-7.79800

3.3.3   Algorithm Output

"Skin" SST is retrieved for all pixels that are not flagged as confident cloudy by the VIIRS cloud mask for all satellite viewing angles. "Bulk" SST is not produced anymore. The data layer, previously used with "bulk" SST is now filled with first guess SST. Quality flags are provided for each pixel to convey the confidence in the cloud screening.

3.4   ALGORITHM SENSITIVITY STUDIES

3.4.1. Comparison of the initial and newly selected SST algorithms

The process of evaluation and selection of the SST algorithm for VIIRS has been described by Petrenko et al. (2013). Here we compare the initial algorithms (4,5) and the selected SST algorithms (8,9) using the dataset of matchups (MDS) collected at STAR from 15 April 2012 to 14 April 2013 and results of SST retrievals from VIIRS observations on 29 April 2013. The MDS includes matchups of VIIRS BTs in bands M12 (3.7 μm), M15 (10.8 μm) and M16 (12 μm) with *in situ* SSTs from the *in situ* Quality Monitor (*i*Quam; *Xu and Ignatov*, [2010], available at www.star.nesdis.noaa.gov/sod/sst/iquam/). Satellite L1b data were processed with the ACSPO, which includes ACSPO Clear-Sky Mask [*Petrenko et al*., 2010] adapted to VIIRS. Along with satellite BTs and *in situ* SST, the MDS includes VZAs, *a priori* SST T_s^0 and total precipitable water vapor content in the atmosphere (TPW, *W*). ACSPO obtains T_s^0 and *W* from gridded DSST and National Center for Environmental Prediction (NCEP) Global Forecast System (GFS, available at www.nco.ncep.noaa.gov/pmb/products/gfs/) products, respectively. T_s^0 and *W* are interpolated from native grids to sensors' pixels, reported in the output L2 files, and saved in the MDS. The time intervals between *in situ* and satellite measurements are ≤2 hours and the distances between buoy's location and the nearest clear-sky pixel are ≤10 km. The total numbers of VIIRS matchups for the 12 month period are 76,971 for daytime and 79,122 for nighttime. Accuracy and precision of satellite SST is characterized with bias, *B*, and standard deviation (SD, *σ*) of T_S with respect to *in situ* SST, T_S^i, averaged over the MDS. It has been shown recently, however, that these statistics may not be fully representative of the quality of SST estimate, because small *B* and *σ* can be in general provided at the expense of suppressing natural SST variability, which would result in underestimation of the SST diurnal variability and spatial gradients [*Merchant et al*., 2009a; *Petrenko et al*., 2011]. To quantitatively characterize the capability of satellite SST to reproduce true SST variations, *Merchant et al*. [2009b] have introduced another metrics – the sensitivity *μ* of retrieved SST to true SST. The *μ* is estimated by differentiating the algorithm's equation in terms of SST, with derivatives of T_B being calculated with RTM. The closer *μ* to 1, the more accurately variations in retrieved SST reproduce true magnitudes of SST variations. The set of three retrieval characteristics, *B, σ* and *μ,* thus more fully characterize the quality of satellite SST estimates.

Regression coefficients for all tested algorithms were derived from the MDS, and SST was estimated for all matchups with the corresponding regression equations. Table 1 shows standard deviations of regression SST minus in situ SST, averaged over the MDS, for the initial and newly selected algorithms, IDPS and OSI-SAF respectively. It should be noted that the matchups used for evaluation of retrieval statistics were selected using the ACSPO Clear-Sky mask. Therefore, the statistics, averaged from matchups selected with more liberal IDPS QC, can differ from those shown in Table 5. The fact that night- and daytime SDs for the OSI-SAF algorithm are remarkably smaller than for the IDPS algorithm, indicates that the OSI-SAF equations (8,9) better approximate the inverse SST-BT relationship than the IDPS equations (4,5).

In addition to average statistics, 2D look-up tables (LUT) were created, in which *B* and *σ* were represented as functions of VZA and TPW by averaging T_S-T_S^i within 10° VZA × 10 kg/m^2 TPW boxes. The corresponding LUT for *μ* was also calculated from one day of VIIRS observations,

29 April 2013, using BT derivatives in terms of SST, calculated within the ACSPO with CRTM. Fig. 8 shows B, σ and μ as functions of VZA at six values of TPW for initial IDPS nighttime algorithm (5) and for OSI-SAF algorithm (9). While the dependencies of σ and μ for both algorithms are similar, the bias for the IDPS algorithm is significantly more variable than the bias in the OSI-SAF SST, and this is the obvious advantage of the OSI-SAF algorithm. Fig, 9 compares the same dependencies for daytime IDPS and OSI-SAF algorithms. As for nighttime algorithms, the daytime IDPS bias is remarkably more variable than for OSI-SAF SST; the SD of IDPS SST is larger than for IDPS SST, especially at large value of TPW. The sensitivity of IDPS SST at small VZAs is more variable than for OSI-SAF SST and, at small TPWs, it significantly exceeds 1.

Table 5. Average standard deviations of retrieved SST with respect to in situ SST over the MDS, for initial (IDPS) and newly selected (OSI-SAF) algorithms.

Algorithm	Night	Day
IDPS	0.384 K	0.471 K
OSI-SAF	0.352 K	0.420 K

Fig. 10 and 11 show composite maps of retrieved SST minus Reynolds SST for IDPS and OSI-SAF algorithms respectively, produced with the ACSPO Clear-Sky Mask (ACSM). Using the same cloud mask for two algorithms helps separate the specific effects of the SST algorithms from the effects of QC and cloud mask. Fig. 10 clearly reveals the cold stripes, corresponding to biases in IDPS SST at large VZAs and TPW. These biases are not visible in Fig. 11, showing the nighttime deviations of OSI-SAF SST from Reynolds SST. The difference between nighttime IDPS and OSI-SAF SSTs is more clearly seen in Fig. 12. The OSI-SAF SST removes biases existing in IDPS SST and therefore it appears to be warmer at large VZAs and TPWs in low latitudes and at small VZAs and small TPW in high latitudes in the Southern Hemisphere (consistently with Fig. 8a). The difference between daytime deviations of IDPS SST and OSI-SAF SST from Reynolds SST is not this noticeable in Fig.13 and 14. However, this difference is clearly seen in Fig. 15, which shows daytime difference between OSI-SAF SST and IDPS SST. This difference shows itself mainly in the regions with large TPWs (tropics) and very low TPWs (as at the coast of Namibia). A certain angular structure of this difference is also noticeable in Fig. 15.

Figure 8. The nighttime retrieval characteristics - (a,b) bias, (c,d) – SD and (e,f) sensitivity to true SST for the initial (IDPS) and newly selected (OSI-SAF) algorithms as functions of view zenith angle, at six values of total precipitable water vapor content in the atmosphere.
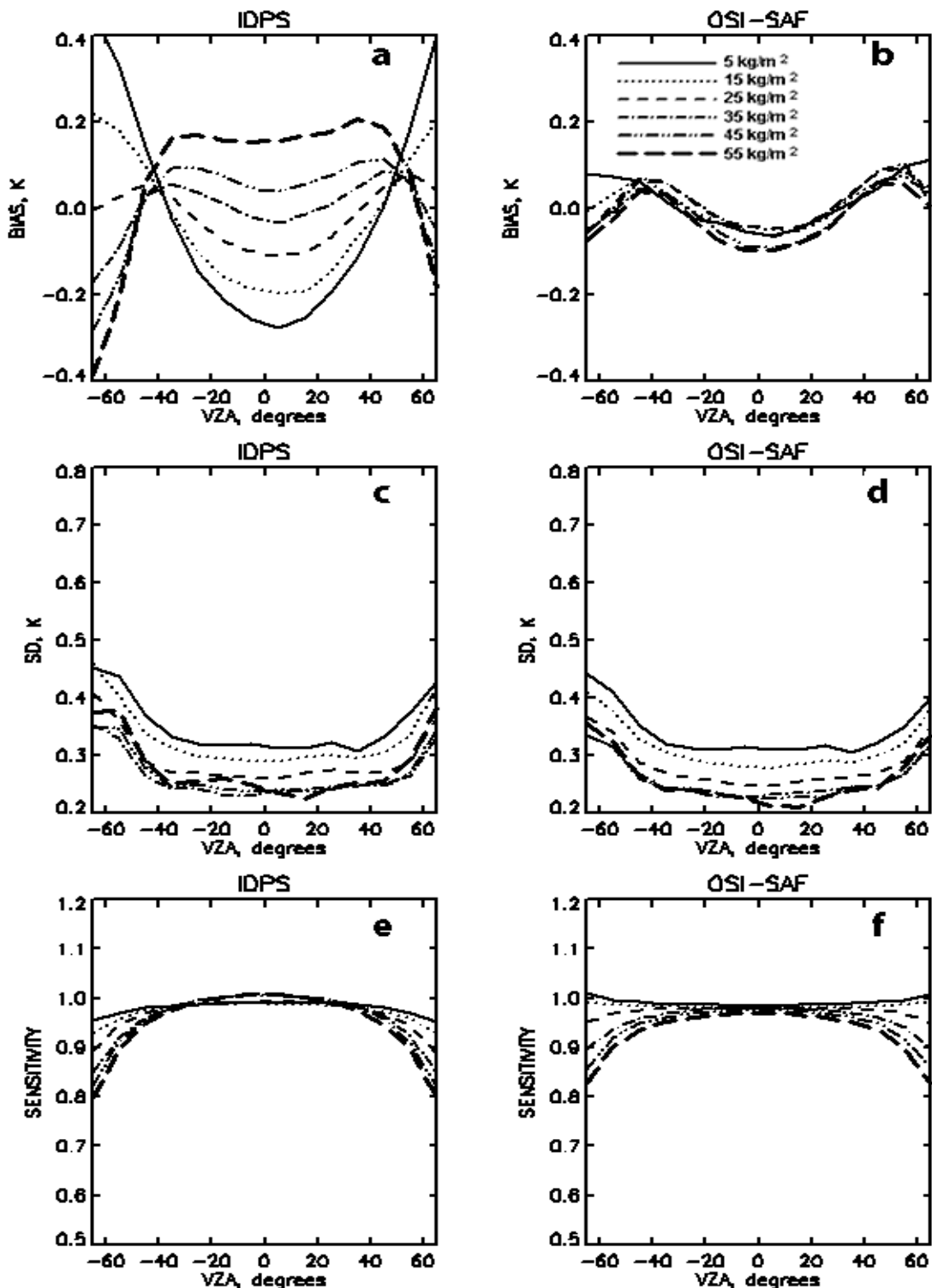
Figure 9. The daytime retrieval characteristics - (a,b) bias, (c,d) – SD and (e,f) sensitivity to true SST for the initial (IDPS) and newly selected (OSI-SAF) algorithms as functions of view zenith angle, at six values of total precipitable water vapor content in the atmosphere.

IDPS_SSTnight
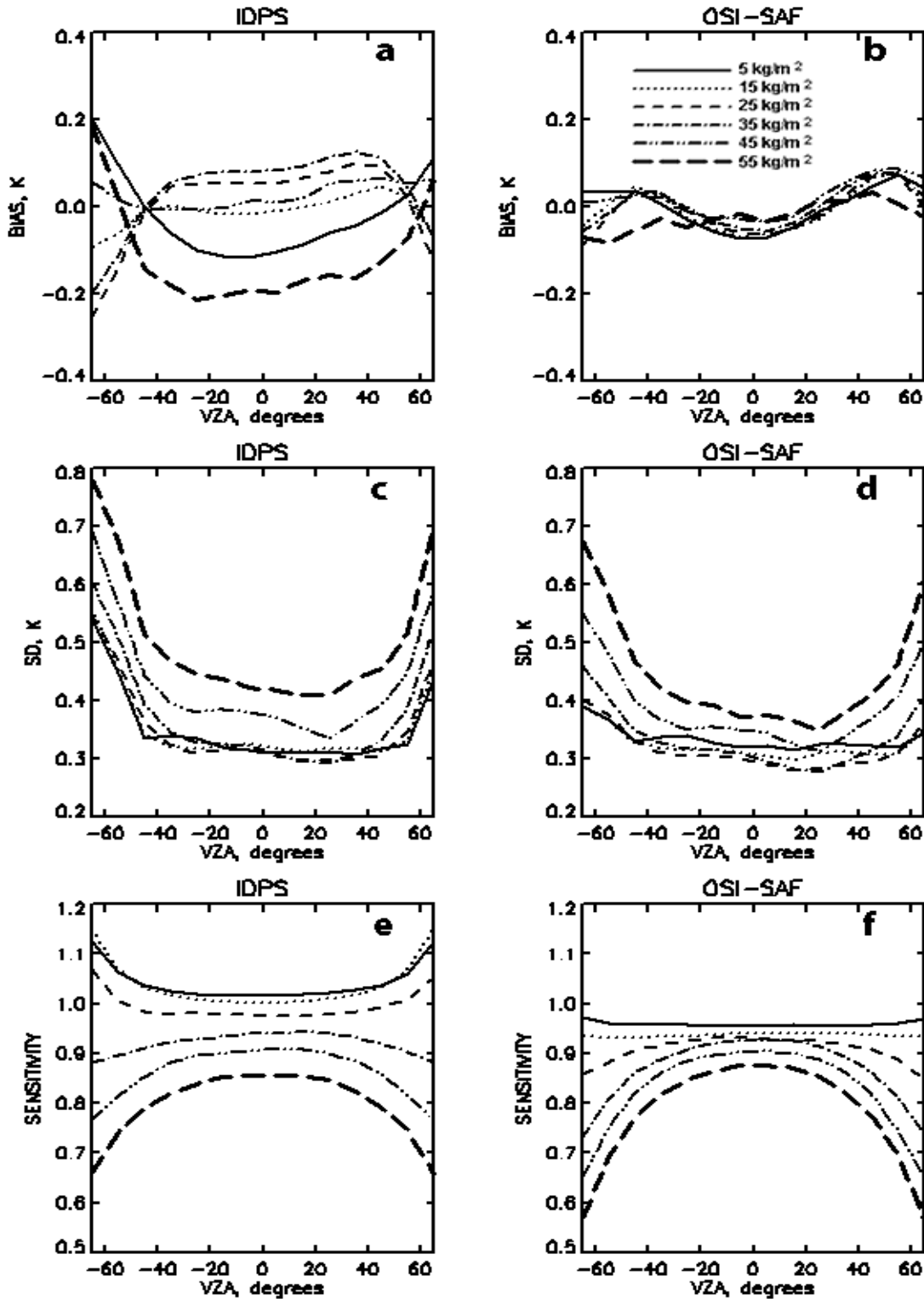

Figure 10. Nighttime composite map of IDPS SST – Reynolds SST produced with the ACSM for 29 April 2013.

OSISAF_SSTnight

Figure 11. Nighttime composite map of OSI-SAF SST – Reynolds SST produced with the ACSM for 29 April 2013.

OSISAF–IDPS_SSTnight

Figure 12. Nighttime composite map of OSI-SAF SST – IDPS SST produced with the ACSM for 29 April 2013.
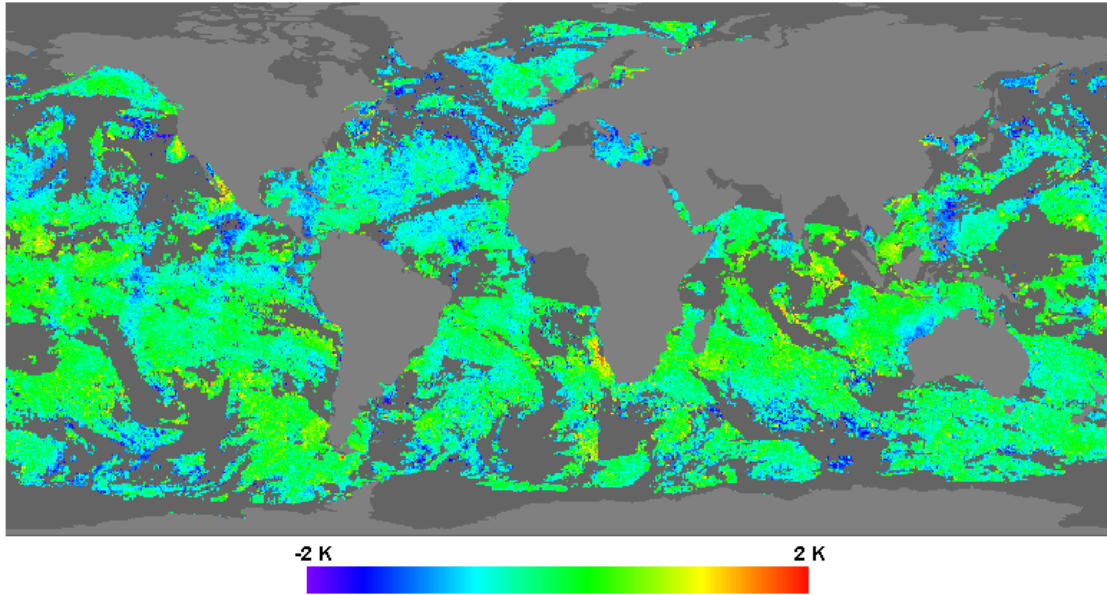
IDPS_SSTday

Figure 13. Daytime composite map of IDPS SST – Reynolds SST produced with the ACSM for 29 April 2013.
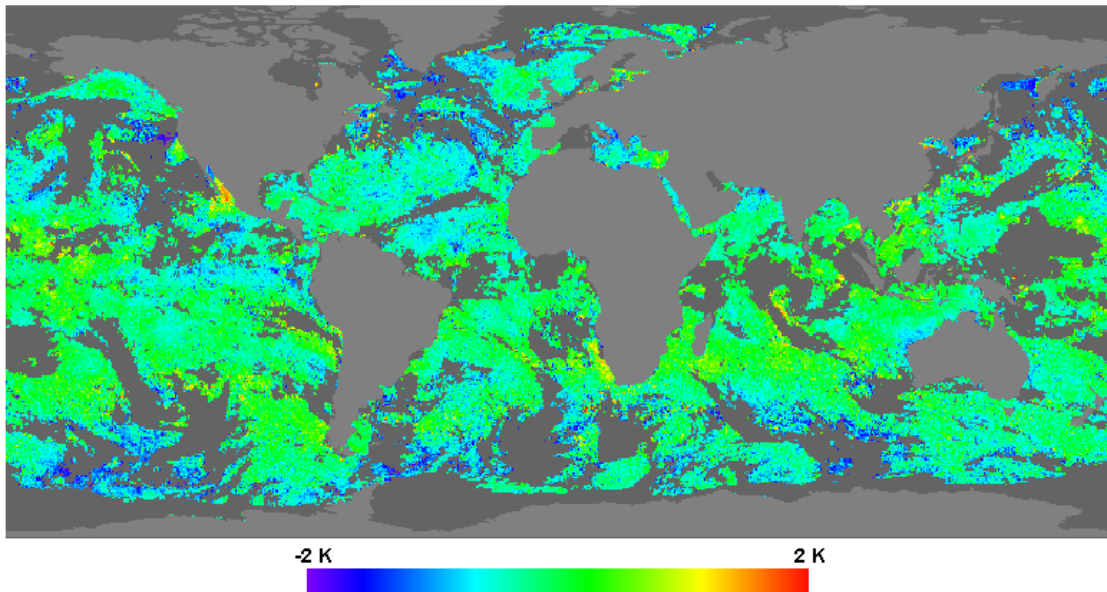
OSISAF_SSTday

Figure 14. Daytime composite map of OSI-SAF SST – Reynolds SST produced with the ACSM for 29 April 2013.
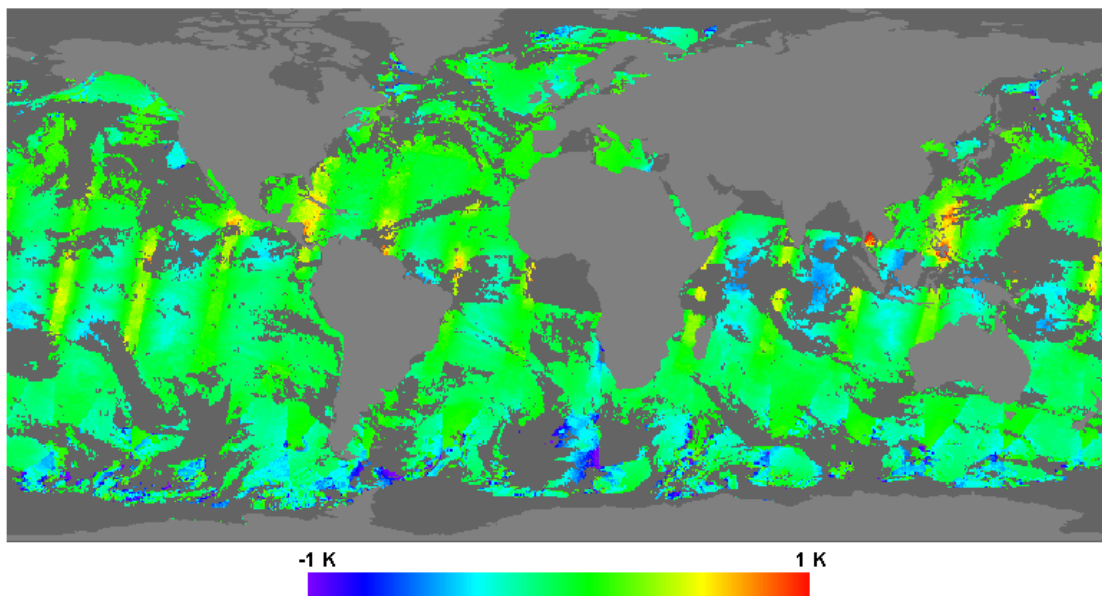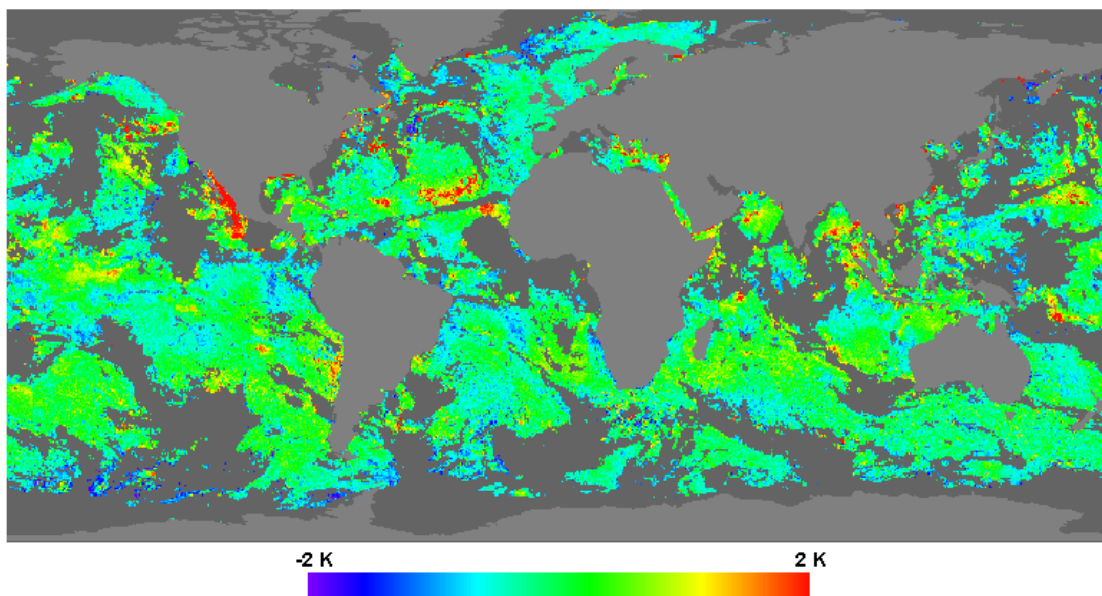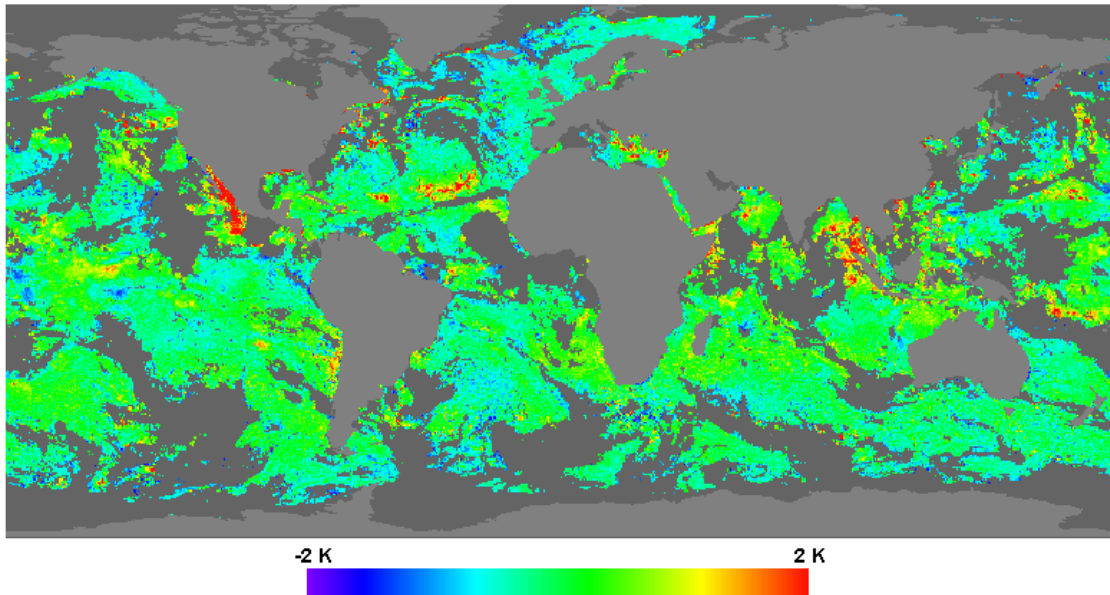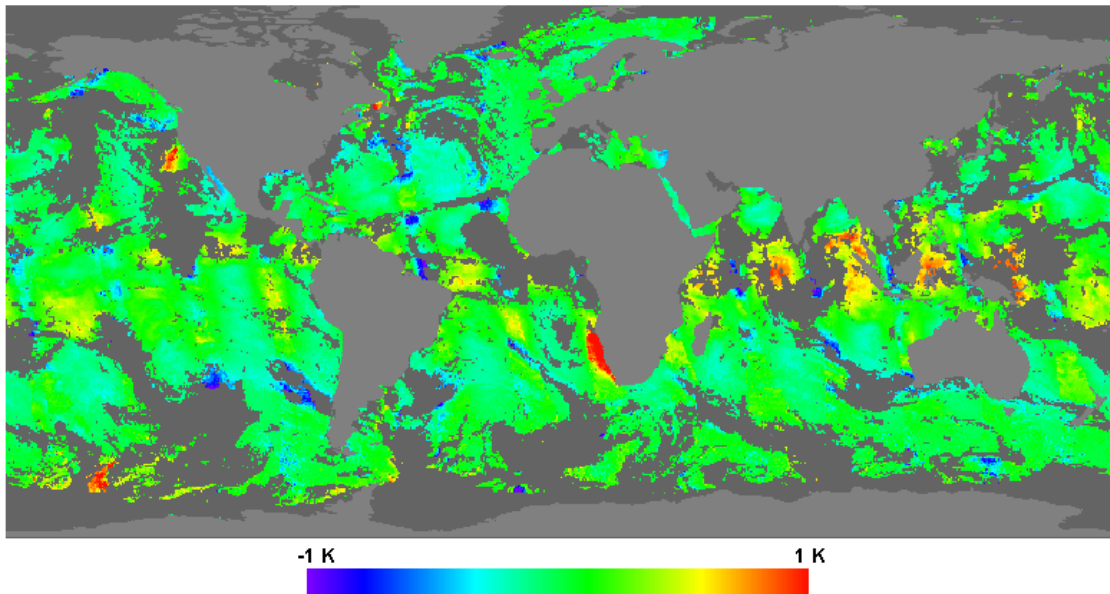
OSISAF—IDPS_SSTday

Figure 15. Daytime composite map of OSI-SAF SST – IDPS SST produced with the ACSM for 29 April 2013.

3.5   PRACTICAL CONSIDERATIONS

3.5.1   Numerical Computation Consideration

In order to retrieve SST within an operational processing environment, statistical algorithms that meet quality requirements have been developed that are much quicker than physical modeling methods. Pre-generated LUTs are used to speed processing yet retain flexibility. This approach has been successfully demonstrated with the MODIS SST retrievals. The revision of the values of LUTs to account for new knowledge of the instrument behavior, including time-dependent degradation of the instrument performance, and new, possibly time dependent, coefficients for the atmospheric correction algorithms, is much easier to achieve than revisions to the computer code. However, some improvements in our understanding of the instrument characteristics and the algorithms' performance, and how to compensate for unanticipated artifacts may still require modifications to the code. The example of the improvement is modification of the algorithm's equations, suggested in this version of ATBD.

3.5.2   Programming and Procedural Considerations

The simplicity of all the algorithms described in this document translates into very small amounts of code using basic mathematical routines. Computationally intensive processes are performed offline, with results delivered as re-generated LUTs.

3.5.3   Configuration of Retrievals

The flexibility built into the architecture also allows easy implementation of possible future developments.

3.5.4   Quality Assessment and Diagnostics

A number of parameters and indicators are reported in the SST product as retrieval diagnostic flags. Statistical information is reviewed for quality assessment. Table 6 lists the available quality flags. The final list of delivered flags will be determined in the operational environment.

Table 6. VIIRS SST EDR Quality Flags

Byte	VIIRS SST Flag	Result	Bits
0	Skin SST quality	11 = High Quality 10 = Degraded 01 = Excluded 00 = Not retrieved	2

Byte	VIIRS SST Flag	Result	Bits
	Spare Bit		1
	Spare Bit		1
	Spare Bit		1
	Spare Bit		1
	Algorithm	1 = Triple Window 0 = Non-linear Split Window	1
	Day / Night	1 = Day 0 = Night	1
1	Bad LWIR SDR	1 = Bad SDR 0 = Good SDR	1
	Bad SWIR SDR	1 = Bad SDR 0 = Good SDR	1
	Cloud Confidence	11 = Confident Cloudy 10 = Probably Cloudy 01 = Probably Clear 00 = Confident Clear	2
	Adjacent Pixel Cloud Confident Value	11 = Confident Cloudy 10 = Probably Cloudy 01 = Probably Clear 00 = Confident Clear	2
	Thin Cirrus	1 = Thin Cirrus 0 = No Thin Cirrus	1
	Sea Ice	1 = Sea Ice 0 = No Sea Ice	1

Byte	VIIRS SST Flag	Result	Bits
2	Sun Glint	1 = Sun glint 0 = No sun glint	1
	Exclusion, AOT > 1	1 = Yes 0 = No	1
	Degraded, AOT > 0.6	1 = Yes 0 = No	1
	Exclusion, Not Ocean	1 = Not ocean 0 = Ocean	1
	Degraded, HCS limit	1 = Past HCS limit 0 = Within HCS limit	1
	Degraded, Sensor Zenith Angle > 40	1 = Yes 0 = No	1
	Skin SST Outside Range	1 = Out of range 0 = In range	1
	Spare Bit		1
3	Skin SST Degraded, T > 305 K	1 = Degraded 0 = Not degraded	1
	Spare Bit		1
	Spare Bit		1
	Spare Bit		1
	Spare Bit		1
	Spare Bit		1
	Spare Bit		1
	Spare Bit		1

3.5.5   Exception Handling

Pixels identified by the cloud mask as confident cloudy are not processed.

3.6   ALGORITHM VALIDATION

3.6.1   Pre-Launch Validation

The pre-launch atmospheric correction algorithm was derived by radiative transfer modeling to simulate the VIIRS TIR channel measurements. Selected radiosondes from the operational network stations or field campaigns were used in the VIIRS simulations for the development of the atmospheric correction algorithm. Measurements from the operational surface drifting and fixed buoy programs were used to characterize the surface temperature fields and to validate the atmospheric correction algorithms. The assimilated NCEP and ECMWF meteorological fields provided a valuable description of the marine atmosphere and surface temperature. These fields were used in conjunction with the radiative transfer modeling to simulate the VIIRS measurements in order to validate the radiosonde data and to provide direct input to the radiative transfer modeling process.

Measurements from AVHRR and ATSR were used in the pre-launch phase to study the error characteristics of the SST retrieval.

3.6.2. Post-launch validation of IDPS EDR SST and comparison with ACSPO SST in SQUAM

The performances of IDPS EDR SST and ACSPO SST have been monitored in SQUAM on a daily basis since stabilization of the VIIRS thermal regime following opening its cryoradiator doors on 18 January 2012. The IDPS and ACSPO systems produce SST using different SST and Quality Control (QC) algorithms, and, therefore the SQUAM results represent the combined effect of SST algorithms and QC. Fig. 16 and 17 show nighttime composite maps of deviations of retrieved SST from L4 Reynolds (2007) Daily High-Resolution Blended SST. The comparison of the two maps shows that the nighttime IDPS EDR SST image contains larger amount of cold SST anomalies. Most of these anomalies are due to the fact that the IDPS QC algorithm is more liberal than the ACSPO Clear-Sky Mask (ACSM Petrenko et al., 2010) and allows more cloud leakages. However, some of those cold anomalies are oriented along swath edges and most likely are caused by the dependency of IDPS EDR SST biases on view zenith angles (cf. Fig. 10 an 12). Fig. 18 and 19 show daytime composite maps of ACSPO SST – Reynolds SST and IDPS EDR SSR – Reynolds, respectively, for the same date. The comparison of Fig. 18 and 19 also shows that the daytime performance of IDPS EDR SST is suboptimal, although it is difficult in this case to separate the deficiencies of SST algorithm from the QC effects. Fig. 20 and 21 show nighttime statistics of ACSPO SST and IDPS EDR SST, respectively. Although the IDPS EDR SST contains 20% more observations than ACSPO SST, this increase is reached at the expense of significant increase of the standard deviation of retrieved SST – Reynolds SST (from 0.43 K to 0.59 K). A similar relationship also takes place for daytime statistics of ACSPO SST and IDPS EDR SST with respect to Reynolds SST, shown in Fig. 22 and 23, respectively: the 20% increase in the number of observations for IDPS EDR is accompanied with growth of SD of retrieved SST – Reynolds SST from 0.56 K to 0.84 K. As was mentioned above, the difference in performances of ACSPO and IDPS SST products has prompted the search of the optimal SST algorithm for VIIRS.

Figure 16. Nighttime composite map of ACSPO SST – Reynolds SST for 29 April 2013.

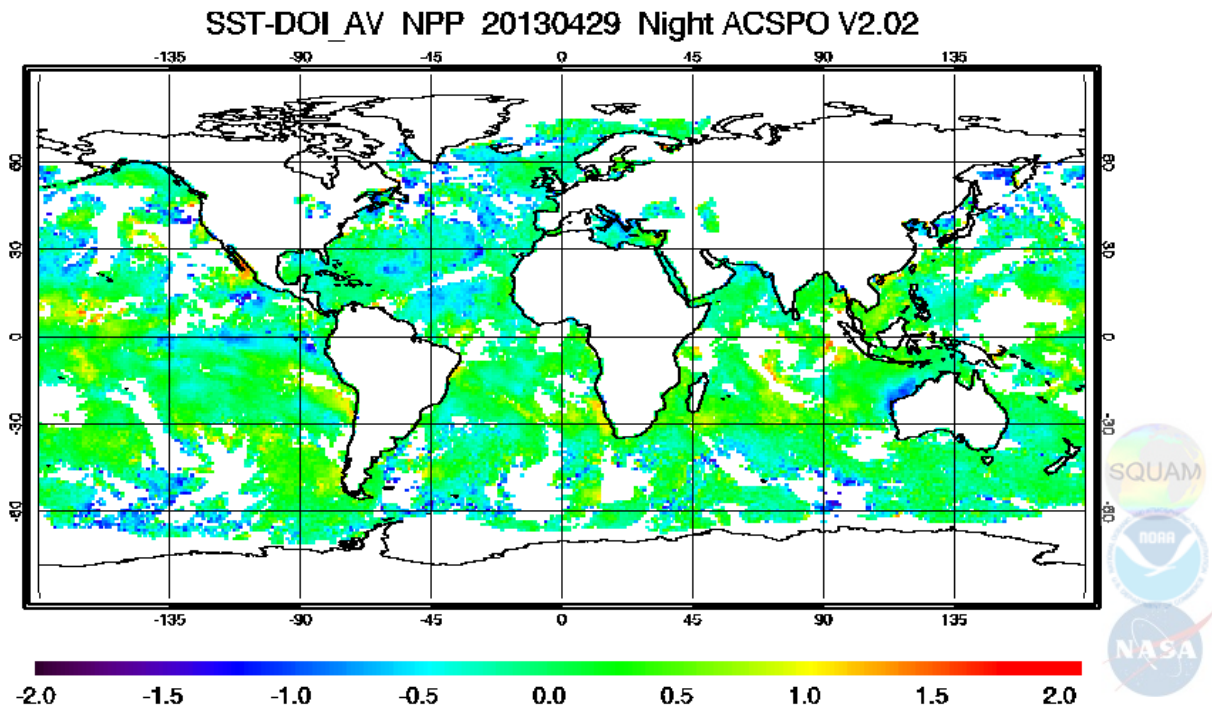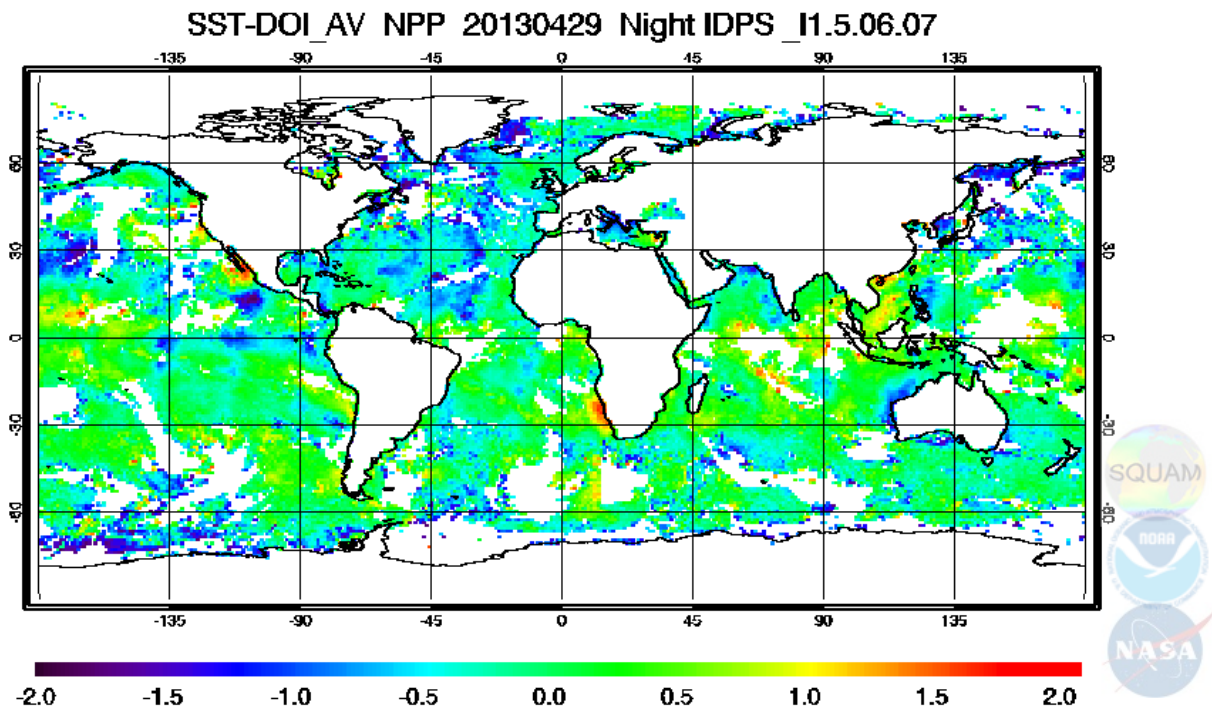**Figure 17. Nighttime composite map of IDPS EDR SST – Reynolds SST for 29 April 2013.**
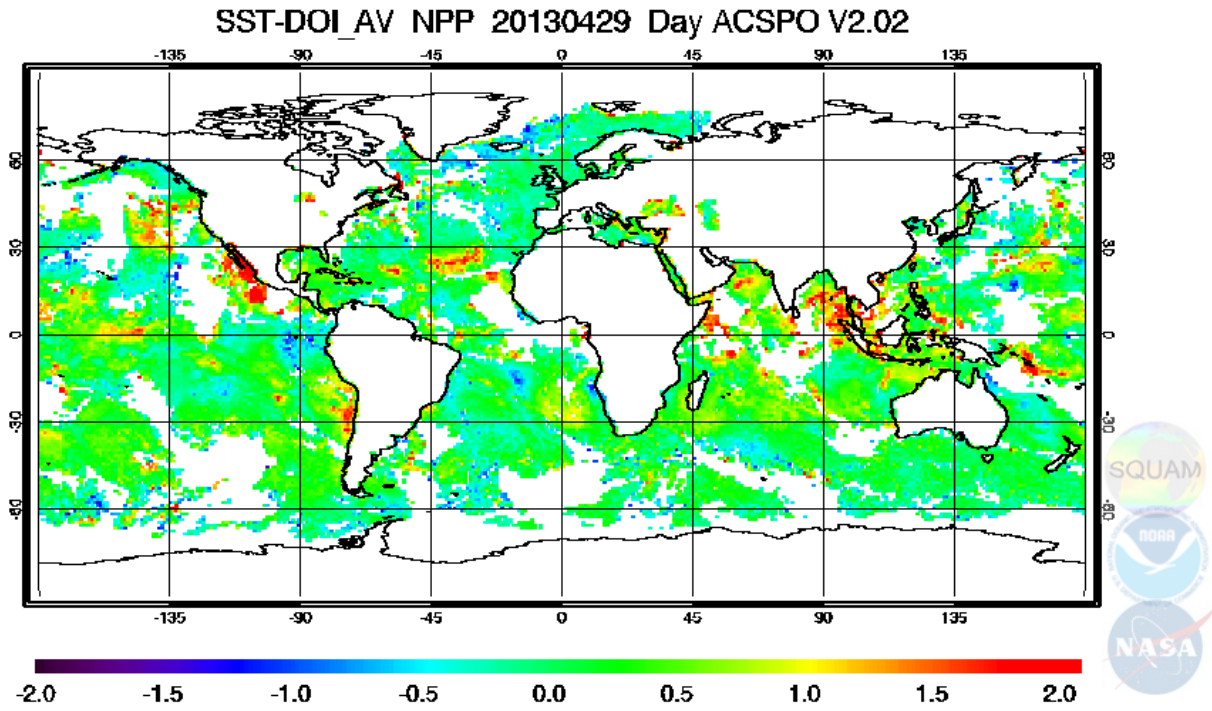
Figure 18. Daytime composite map of ACSPO SST – Reynolds SST for 29 April 2013.

Figure 19. Daytime composite map of IDPS EDR SST – Reynolds SST for 29 April 2013.

Figure 20. Nighttime statistics of ACSPO SST – Reynolds SST for 29 April 2013.

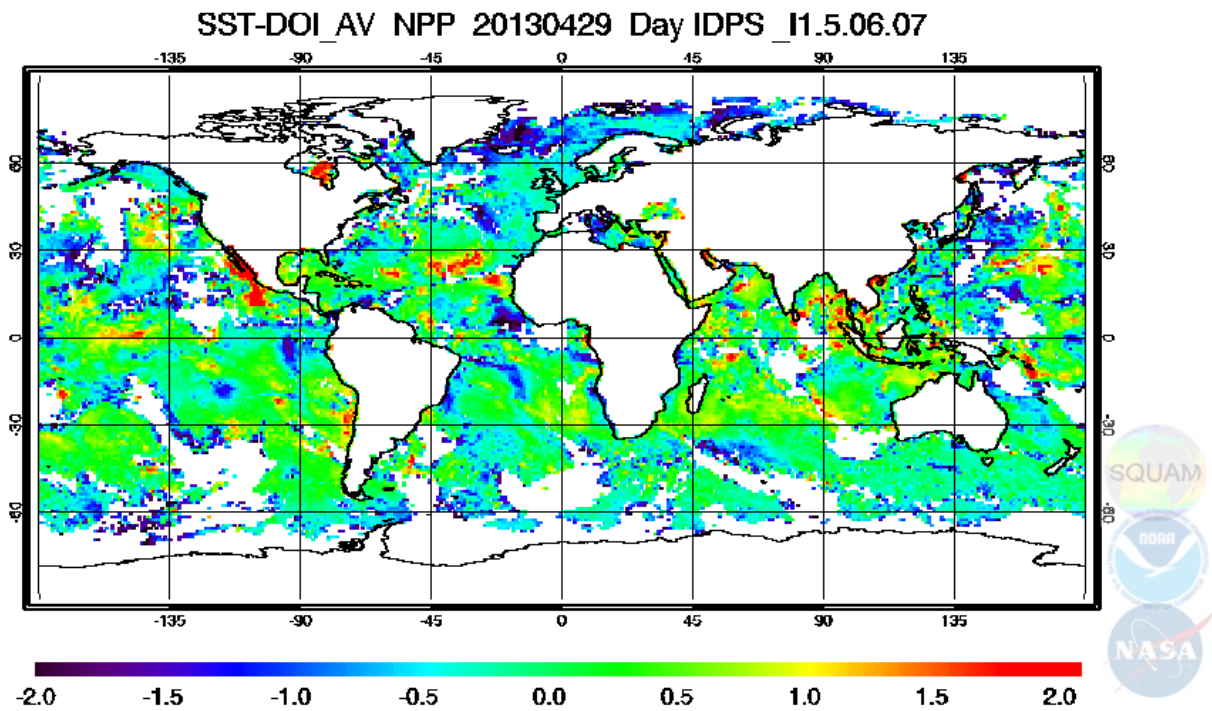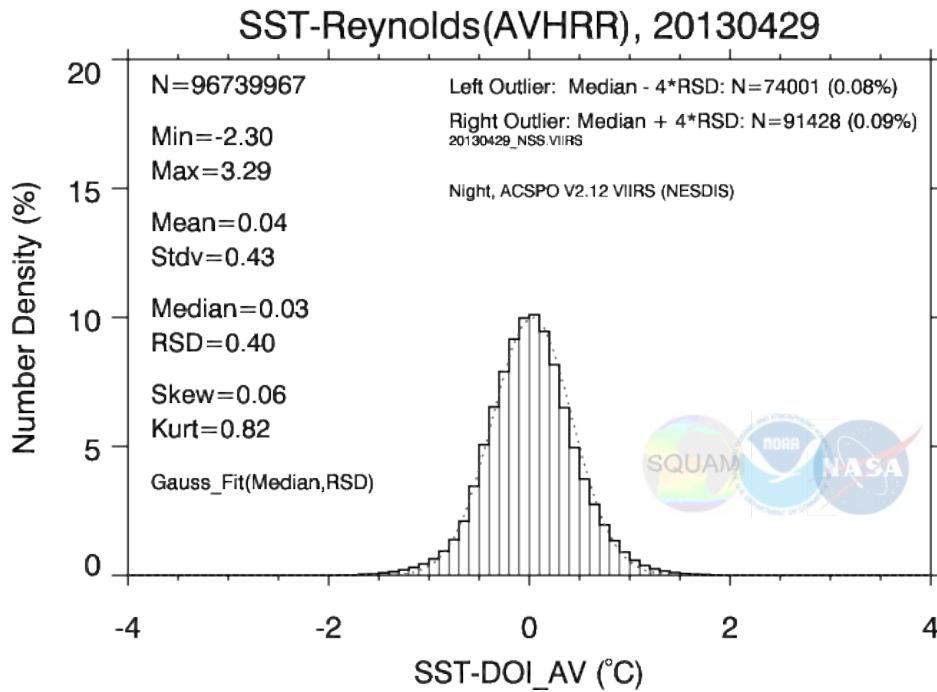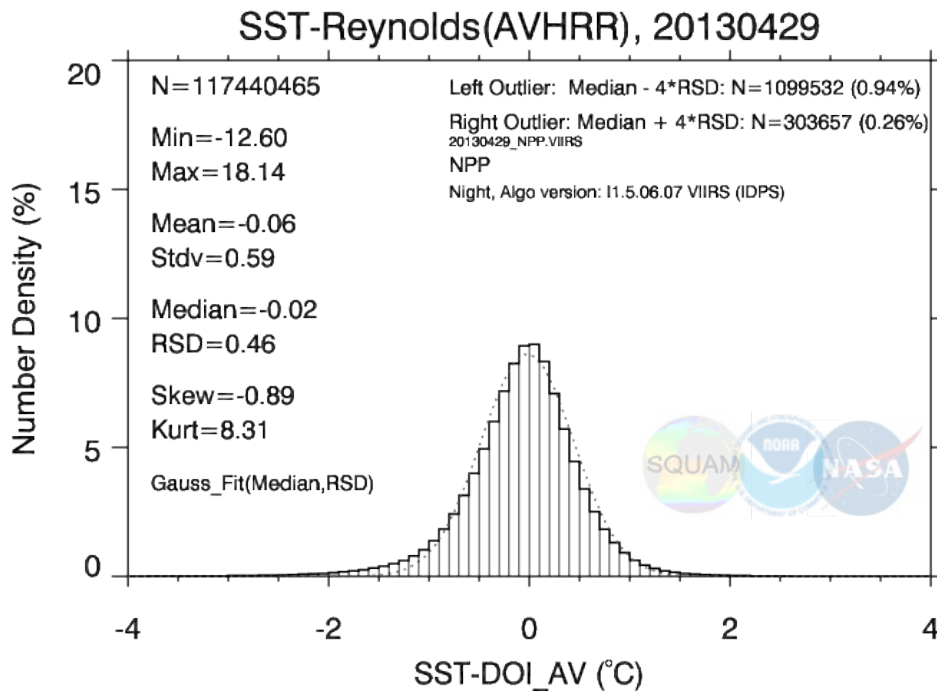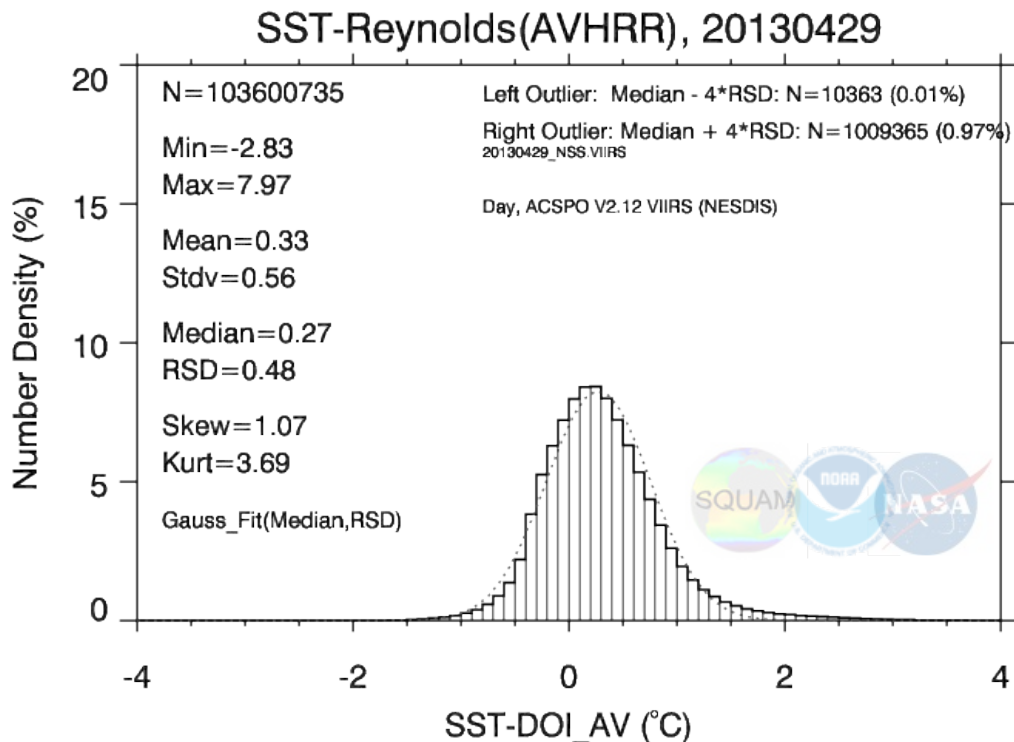**Figure 21. Nighttime statistics of IDPS EDR SST – Reynolds SST for 29 April 2013.**

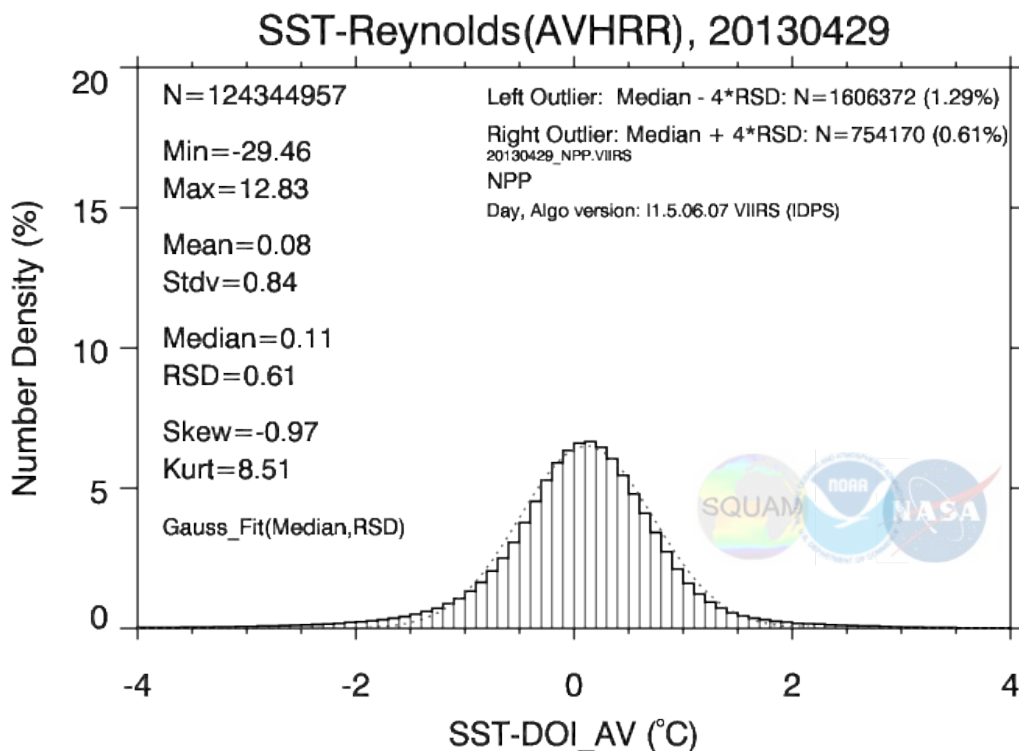**Figure 22. Daytime statistics of ACSPO SST – Reynolds SST for 29 April 2013.**

Figure 23. Daytime statistics of ACSPO SST – Reynolds SST for 29 April 2013.

3.7 ALGORITHM DEVELOPMENT SCHEDULE

At the time of writing, the base-line algorithms have been tested and delivered.

4.0   ASSUMPTIONS AND LIMITATIONS

4.1   SENSOR PERFORMANCE

The VIIRS SST retrieval is feasible only under clear sky conditions; this is a limitation common to all infrared remote sensing of the surface temperatures from satellites. Another limitation on the accuracy of the SST retrievals results from the effects of increasing atmospheric path length at large scan angles. The VIIRS SST retrievals will be most accurate near the center of the swath.

4.2   Derivation of Bulk SST from Skin SST

The structure of VIIRS EDR developed prior to VIIRS launch included separate layers for "skin" and "bulk" SST, which differed from each other by a constant offset of 0.17 K. In the current version of VIIRS EDR, only "skin" SST is represented. Users can easily produce "bulk" SST from "skin" SST by adding 0.17 K or by using more sophisticated "skin/bulk" algorithms, which can be developed in the future. The vacant layer is now used to output first guess SST, which significantly simplifies the process of validation of the VIIRS SST product.

4.3   Physical SST Retrieval

A common limitation of all regression SST algorithms, including those suggested in this ATBD, is significant non-uniformity of accuracy and precision of retrieved SST over the range of possible observational conditions. As alternatives to regression, several SST algorithms based on radiative transfer model (RTM) have been recently developed [*Merchant et al*, 2009a; *Le Borgne et al*., 2011; *Petrenko et al*., 2011] and shown to provide more uniform SST accuracy and precision. However, implementation of RTM-based algorithms is more complex than for regression, mainly because they require on-line radiative transfer computations. In particular, the Incremental Regression algorithm [*Petrenko et al*., 2011] is currently being tested in ACSPO, which incorporates the Community Radiative Transfer Model [*Liang et al*., 2009; *Liang and Ignatov*, 2011, 2013]. On the other hand, only regression algorithms can be implemented within the IDPS system because the IDPS currently does not support on-line RTM simulations.

5.0   REFERENCES

Barton, I. J., A. J. Prata, and D. T. Llewellyn-Jones (1993).   Adv. Space Res., 69., 1993: The Along Track Scanning Radiometer – an Analysis of coincident ship and satellite measurements. *Advances in Space Research*, **13,** 69-74.doi:10.1016/0273-1177(93)90529-K

Barton, I. J., P. J. Minnett, C. J. Donlon, S. J. Hook, A. T. Jessup, K. A. Maillet, and T. J. Nightingale, 2004: The Miami2001 infrared radiometer calibration and inter-comparison: 2. Ship comparisons. *Journal of Atmospheric and Oceanic Technology*, **21,** 268-283

Berk, A., L. S. Bemstein, and D. C. Robertson, 1989: MODTRAN: A moderate resolution model for LOWTRAN 7. Spectral Sciences, Inc. Burlington, MA.

Branch, R., A. T. Jessup, P. J. Minnett, and E. L. Key, 2008: Comparisons of Shipboard Infrared Sea Surface Skin Temperature Measurements from the CIRIMS and the M-AERI. *Journal of Atmospheric and Oceanic Technology*, **25,** 598-606.doi: 10.1175/2007JTECHO480.1

Brisson, A., P. Le Borgne, and A. Marsouin (2002), Result of one year of preoperational production of Sea Surface Temperatures from GOES-8, *J. Atmos. Oceanic Technol.*, **19** (*10*), 1638–1652.Brown, O. B. and P. J. Minnett, 1996: MODIS Infrared Sea Surface Temperature Algorithm Algorithm Theoretical Basis Document, Version 2.0.

Casey, K. S. and P. Cornillon, 1999: A Comparison of Satellite and In Situ-Based Sea Surface Temperature Climatologies. *Journal of Climate*, **12,** 1848-1863.

Castro S.L., G.A.Wick, P.J. Minett, A.T. Jessup, & W.J. Emery, 2010: The impact of measurement uncertainty and spatial variability on the accuracy of skin and subsurface regression-based sea surface temperature algorithms. *RSE*, 114, 2666-2678.

Chen, S. S. and R. A. Houze, 1997: Diurnal variation and lifecycle of deep convective systems over the tropical Pacific warm pool. *Quarterly Journal of the Royal Meteorological Society*, **123,** 357-388

Chesters, D., L. W. Uccellini, and W. D. Robinson, 1983: Low-level water vapor fields from the VISSR Atmospheric Sounder (VAS) "split window" channels. *Journal of Climate and Applied Meteorology*, **22,** 725-743

Clough, S. A., F. X. Kneizys, and R. W. Davies, 1989: Line shape and the water vapor continuum. *Atmos. Res.*, **23,** 229-241

Cornette, W. M., P. K. Acharya, D. C. Robertson, and G. P. Anderson, 1994: Moderate spectral atmospheric radiance and transmittance code (MOSART). Photon Research Associates, Inc. La Jolla, CA.

Dash, P., Ignatov, A., Kihai, Y., Sapper, J. (2010), The SST Quality Monitor (SQUAM), *J. Atmos. Oceanic Technol.*, **27,** 1899–1917. doi: 10.1175/2010JTECHO756.1.Donlon, C., I. S. Robinson, M. Reynolds, W. Wimmer, G. Fisher, R. Edwards, and T. J. Nightingale, 2008: An Infrared Sea Surface Temperature Autonomous Radiometer (ISAR) for Deployment aboard Volunteer Observing Ships (VOS). *Journal of Atmospheric and Oceanic Technology*, **25,** 93-113

Donlon, C., I. Robinson, K. S. Casey, J. Vazquez-Cuervo, E. Armstrong, O. Arino, C. Gentemann, D. May, P. LeBorgne, J. Piollé, I. Barton, H. Beggs, D. J. S. Poulter, C. J. Merchant, A. Bingham, S. Heinz, A. Harris, G. Wick, B. Emery, P. Minnett, R. Evans, D. Llewellyn-Jones, C. Mutlow, R. W. Reynolds, H. Kawamura, and N. Rayner, 2007: The

Global Ocean Data Assimilation Experiment High-resolution Sea Surface Temperature Pilot Project. *Bulletin of the American Meteorological Society*, **88,** 1197-1213

Donlon, C. J., T. Nightingale, L. Fiedler, G. Fisher, D. Baldwin, and I. S. Robinson, 1999: The Calibration and Intercalibration of Sea-Going Infrared Radiometer Systems Using a Low Cost Blackbody Cavity. *Journal of Atmospheric and Oceanic Technology*, **16,** 1183–1197

Donlon, C. J., P. J. Minnett, C. Gentemann, T. J. Nightingale, I. J. Barton, B. Ward, and J. Murray, 2002: Toward improved validation of satellite sea surface skin temperature measurements for climate research. *Journal of Climate*, **15,** 353-369

Emery, W., Y. Yu, G. Wick, P. Schluessel, and R. W. Reynolds, 1994: Correcting infrared satellite estimates of sea surface temperature for atmospheric water vapor attenuation. *J. Geophys. Res.*, **99,** 5219-5236

Fowler, J. B., 1995: A third generation water bath based blackbody source. *J. Res. Natl.Inst. Stand. Technol.*, **100,** 591-599

Gentemann, C. L. and P. J. Minnett, 2008: Radiometric measurements of ocean surface thermal variability. *Journal of Geophysical Research*, **113,** C08017.doi:10.1029/2007JC004540

Gentemann, C. L., P. J. Minnett, and B. Ward, 2008a: Profiles of Ocean Surface Heating (POSH): a new model of upper ocean diurnal thermal variability. *Journal of Geophysical Research***,** In review

Gentemann, C. L., C. J. Donlon, A. Stuart-Menteth, and F. J. Wentz, 2003: Diurnal signals in satellite sea surface temperature measurements. *Geophysical Research Letters*, **30,** 1140-1143

Gentemann, C. L., P. J. Minnett, P. LeBorgne, and C. J. Merchant, 2008b: Multi-satellite measurements of large diurnal warming events. *Geophysical Research Letters***,** In the press.doi:10.1029/2008GL035730

Good, S. A., G. K. Corlett, J. J. Remedios, E. J. Noyes, and D. T. Llewellyn-Jones, 2007: The Global Trend in Sea Surface Temperature from 20 Years of Advanced Very High Resolution Radiometer Data. *Journal of Climate*, **20,** 1255-1264.doi: 10.1175/JCLI4049.1

Han, Y., J. A. Shaw, J. H. Churnside, P. D. Brown, and S. A. Clough, 1997: Infrared spectral radiance measurements in the tropical Pacific atmosphere. *Journal of Geophysical Research*, **102,** 4353-4356

Hanafin, J. A. and P. J. Minnett, 2005: Infrared-emissivity measurements of a wind-roughened sea surface. *Applied Optics.*, **44,** 398-411

Hasse, L., 1971: The sea surface temperature deviation and the heat flow at the sea-air interface. *Boundary-Layer Meteorology*, **1,** 368-379

Horrocks, L. A., B. Candy, T. J. Nightingale, R. W. Saunders, A. O'Carroll, and A. R. Harris, 2003: Parameterizations of the ocean skin effect and implications for satellite-based measurement of sea-surface temperature. *Journal of Geophysical Research*, **108,** 3096

Ignatov, A., J. Sapper, J. , I. Laszlo, et al., (2004), Global operational SST and aerosol products from AVHRR: current status, diagnostics, and potential enhancements. 13th Conf. Satellite Meterology and Oceanography, Norfolk, VA, 20-23 September 2004. http://www.star.nesdis.noaa.gov/smcd/emb/aerosol/ignatov/conf/2004-AMS-13ConfSatMetOcean-IgnatovEtAl-AVHRRSSTAerosol-Poster.pdf

Ignatov A., J. Sapper, Y. Kihai, et al., (2012), Polar SST Products and Monitoring at NESDIS. 13th GHRSST meeting, 4-8 June 2012, Tokyo, Japan. https://www.ghrsst.org/files/download.php?m=documents&f=120611145909-1120120604ACSPOMonitoringIgnatovv04.pdf

Jessup, A. T. and R. Branch, 2008: Integrated Ocean Skin and Bulk Temperature Measurements Using the Calibrated Infrared In Situ Measurement System (CIRIMS) and Through-Hull Ports. *Journal of Atmospheric and Oceanic Technology*, **25,** 579-597.DOI: 10.1175/2007JTECHO479.1

Kalnay, E., M. Kanamitsu, R. Kistler, W. Collins, D. Deaven, L. Gandin, M. Iredell, S. Sha, G. White, J. Woollen, Y. Zhu, M. Chelliah, W. Ebisuzaki, W. Higgins, J. Janowiak, K. C. Mo, C. Ropelewski, J. Wang, A. Leetmaa, R. Reynolds, R. Jenne, and D. Joseph, 1996: The NCEP/NCAR 40-Year Reanalysis Project. *Bulletin of the American Meteorological Society*, **77,** 437-471

Kannenberg, R., 1998: IR instrument comparison workshop at the Rosenstiel School of Marine and Atmospheric Science (RSMAS). *The Earth Observer*, **10,** 51-54

Kearns, E. J., J. A. Hanafin, R. H. Evans, P. J. Minnett, and O. B. Brown, 2000: An independent assessment of Pathfinder AVHRR sea surface temperature accuracy using the Marine-Atmosphere Emitted Radiance Interferometer (M-AERI). *Bulletin of the American Meteorological Society*, **81,** 1525-1536

Kilpatrick, K. A., G. P. Podestá, and R. H. Evans, 2001: Overview of the NOAA/NASA Pathfinder algorithm for Sea Surface Temperature and associated Matchup Database. *Journal of Geophysical Research*, **106,** 9179-9198

Kneizys, F. X., E. P. Shettle, L. W. Abreu, J. H. Chetwynd, G. P. Anderson, W. O. Gallery, J. E. A. Selby, and S. A. Clough, 1988: Users Guide to LOWTRAN 7. Air Force Geophysics Laboratory Bedford, MA.

Lavanant, L., P. Le Borgne, G. Legendre, A. Marsouin, S. Pere, and H. Roquet (2012), VIIRS SST at OSI-SAF. GHRSST XIII Science Team Meeting, Tokyo, https://www.ghrsst.org/files/download.php?m=documents&f=120618134746-GHRSSTXIIIviirsosisaf3.pdf

Le Borgne, P., H. Roquet, and C.J. Merchant, 2011: Estimation of sea surface temperature from the Spinning Enhanced Visible and Infrared Imager, improved using numerical weather prediction, *Remote Sens. of Environment.*, **115**, 55–65.Legeckis, R. and T. Zhu, 1997: Sea surface temperature from the GEOS-8 geostationary satellite. *Bull. Amer. Meteor. Soc.*, **78,** 1971-1983

Liang, X., and A. Ignatov (2011), Monitoring of IR Clear-sky Radiances over Oceans for SST (MICROS). *J. Atmos. Ocean. Technol., ***28***,* doi:10.1175/JTECH-D-10-05023.1.

Liang, X. and A. Ignatov (2013), AVHRR, MODIS and VIIRS radiometric stability and consistency in SST bands. *J. Geophys. Res.*, in press

Masuda, K., T. Takashima, and Y. Takayama, 1988: Emissivity of pure and sea waters for the model sea surface in the infrared window region. *Rem. Sens. of Environment*, **24,** 313-329

May, D. A., M. M. Parmeter, D. S. Olszewski, and B. D. McKenzie, 1998: Operational processing of satellite sea surface temperature retrievals at the Naval Oceanographic Office. *Bulletin of the American Meteorological Society*, **79,** 397-407

McClain, E. P., W. G. Pichel, C. C. Walton, Z. Ahmad, and J. Sutton, 1983: Multi-channel improvements satellite derived global sea surface temperatures. *Adv. Space Res.*, **2,** 43-47

McMillin, L., 1975: Estimation of sea-surface temperatures from two infrared window measurements with different absorption. *J. Geophys. Research*, **80,** 5113-5117

Merchant, C. J., A. R. Harris, J. Murray, and A. M. Zavody, 1999: Toward the elimination of bias in satellite retrievals of skin sea surface temperature. 1: Theory. modelling and inter-algorithm comparison. *J. Geophys. Res.*, **104,** 23565-23578

Merchant, C. J., P. LeBorgne, A. Marsouin, and H. Roquet, 2008: Optimal estimation of sea surface temperature from split-window observations. *Remote Sensing of Environment*, **112,** 2469-2484

Merchant, C. J., P. Le Borgne, P., H. Roquet, and A. Marsouin (2009a), Sea surface temperature from a geostationary satellite by optimal estimation, *Remote Sens. Environ.*, **113**, 445–457.

Merchant, C.J., A. R. Harris, H. Roquet, and P. Le Borgne (2009b), Retrieval characteristics of non-linear sea surface temperature from the Advanced Very High Resolution Radiometer. *Geophys. Res. Lett.*, **36**, *L17604*, doi: 10.1029/2009GL039843.

Minnett, P. J., 2003: Radiometric measurements of the sea-surface skin temperature - the competing roles of the diurnal thermocline and the cool skin. *International Journal of Remote Sensing*, **24,** 5033-5047

Minnett, P. J., M. Smith, and B. Ward, 2008: Measurements of the oceanic thermal skin effect. *Deep Sea Research II*, **Submitted**

Minnett, P. J., R. O. Knuteson, F. A. Best, B. J. Osborne, J. A. Hanafin, and O. B. Brown, 2001: The Marine-Atmospheric Emitted Radiance Interferometer (M-AERI), a high-accuracy, sea-going infrared spectroradiometer. *Journal of Atmospheric and Oceanic Technology*, **18,** 994-1013

Mutlow, C. T., D. T. Llewellyn-Jones, A. M. Závody, and I. J. Barton, 1994: Sea-surface temperature measurements by the Along-Track Scanning Radiometer (ATSR) on ESA's ERS-1 Satellite - Early results. *J. Geophys. Res.*, 22,575-22,588

Nalli, N. R., P. J. Minnett, and P. van Delst, 2008a: Emissivity and reflection model for calculating unpolarized isotropic water surface-leaving radiance in the infrared. I: Theoretical development and calculations. *Applied Optics*, **47,** 3701-3721.doi:10.1364/AO.47.003701

Nalli, N. R., P. J. Minnett, E. Maddy, W. W. McMillan, and M. D. Goldberg, 2008b: Emissivity and reflection model for calculating unpolarized isotropic water surface-leaving radiance in the infrared. 2: Validation using Fourier transform spectrometers. *Applied Optics*, **47,** 4649-4671.doi:10.1364/AO.47.004649

Noyes, E. J., P. J. Minnett, J. J. Remedios, G. K. Corlett, S. A. Good, and D. T. Llewellyn-Jones, 2006: The Accuracy of the AATSR Sea Surface Temperatures in the Caribbean. *Remote Sensing of Environment*, **101,** 38-51

OSI-SAF Low Earth Orbiter Sea Surface Temperature Product User Manual, Version 2.1. The EUMETSAT Network of Satellite Application Facilities, OSI-SAF (2009), http://www.osi-saf.org/biblio/docs/ss1_pum_leo_sst_2_1.pdf

Petrenko, B., A. Ignatov, Y. Kihai, and A. Heidinger (2010), Clear-sky mask for the Advanced Clear-Sky Processor for Oceans, *J. Atmos. Oceanic Technol.*, **27**, 1609–1623.

Petrenko, B., A. Ignatov, N. Shabanov, and Y. Kihai (2011), Development and evaluation of SST algorithms for GOES-R ABI using MSG SEVIRI as a proxy, *Remote Sens. Environ.*, **115**, 3647–3658.

Petrenko, B., A. Ignatov, and Y. Kihai (2013), Evaluation and selection of SST regression algorithms for VIIRS, *Journal of Geophysical Research*, submitted.

Reynolds, R.W., T.M. Smith, C. Liu, C., D.B. Chelton, K.S. Casey, and M.G. Schlax (2007), Daily high-resolution-blended analyses for sea surface temperature, *J. Clim.*, **20**, 5473–5496.

Rice, J. P. and B. C. Johnson, 1998: The NIST EOS Thermal-Infrared Transfer Radiometer. *Metrologia*, **35,** 505-509

Rice, J. P., J. J. Butler, B. C. Johnson, P. J. Minnett, K. A. Maillet, T. J. Nightingale, S. J. Hook, A. Abtahi, C. J. Donlon, and I. J. Barton, 2004: The Miami2001 Infrared Radiometer Calibration and Intercomparison: 1. Laboratory Characterization of Blackbody Targets. *J. Atm. Ocean. Tech.*, **21,** 258-267

Saunders, P. M., 1967: The temperature at the ocean-air interface. *J. Atmos. Sci.*, **24,** 269-274

Schluessel, P., W. J. Emery, H. Grassl, and T. Mammen, 1990: On the bulk-skin temperature difference and its impact on satellite remote sensing of sea surface temperatures. *Journal of Geophysical Research*, **95,** 13,341-13,356

Smith, A. H., R. W. Saunders, and A. M. Závody, 1994: The validation of ATSR using aircraft radiometer data over the Tropical Atlantic. *J. Atmos. and Oceanogr. Techn.*, **11,** 789-800

Sobrino, J. A., J. E. Kharraz, and Z.-L. Li, 2003: Surface temperature and water vapour retrieval from MODIS data *International Journal of Remote Sensing*, **24,** 5161-5182.doi: 10.1080/0143116031000102502

Soloviev, A. V. and P. Schlüssel, 1994: Parameterization of the cool skin of the ocean and of the air-ocean gas transfer on the basis of modeling surface renewal. *J. Phys. Oceanogr*, **24,** 1339-1346.

Soloviev, A. V. and P. Schlüssel, 1996: Evolution of cool skin and direct air-sea gas transfer coefficient during daytime. *Bound.-Layer Meteor.*, **77,** 45-68

Stephens, G. L., 1990: On the relationship between water vapor over the oceans and sea surface temperature. *Journal of Climate*, **3,** 634-645

Stuart-Menteth, A., I. S. Robinson, and P. G. Challenor, 2003: A global study of diurnal warming using satellite-derived sea surface temperature. *J. Geophys. Res.*, **108,** 3155

Stuart-Menteth, A. C., I. S. Robinson, and C. J. Donlon, 2005a: Sensitivity of the diurnal warm layer to meteorological fluctuations. Part 2: A new parameterisation for diurnal warming. *Journal of Atmospheric and Ocean Science*, **10,** 209-234

Stuart-Menteth, A. C., I. S. Robinson, R. A. Welller, and C. J. Donlon, 2005b: Sensitivity of the diurnal warm layer to meteorological fluctuations part 1: observations. *Journal of Atmospheric and Ocean Science*, **10,** 193-208

Walton, C. C., 1988: Nonlinear multichannel algorithms for estimating sea surface temperature with AVHRR satellite data. *Journal of Applied Meteorology*, **27,** 115-124

Walton, C. C., W. G. Pichel, J. F. Sapper, and D. A. May, 1998: The development and operational application of nonlinear algorithms for the measurement of sea surface temperatures with the NOAA polar-orbiting environmental satellites. *Journal of Geophysical Research*, **103,** 27,999-28,012

Ward, B., 2006: Near-Surface Ocean Temperature. *Journal of Geophysical Research*, **111,** C02005

Watts, P., M. Allen, and T. Nightingale, 1996: Sea surface emission and reflection for radiometric measurements made with the along-track scanning radiometer. *Journal of Atmospheric and Ocean Technology*, **13,** 126-141

Webster, P. J., C. A. Clayson, and J. A. Curry, 1996: Clouds, radiation, and the diurnal cycle of sea surface temperature in the tropical western Pacific. *Journal of Climate*, **9,** 1712-1730

Wick, G., J. Bates & D. Scott, 2002: Satellite and skin-layer effects on the accuracy of SST measurements from the GOES satellites. *JTech*, 19, 1834-1847.Williams, E., E. Prager, and D. Wilson, 2002: Research Combines with Public Outreach on a Cruise Ship. *EOS*, **83,** 590, 596.

Woods, S., P. J. Minnett, and C. L. Gentemann, 2008: Influence of the cool skin layer on global air-sea CO_2 flux estimates. *In preparation*

Wu, X. and W. L. Smith, 1997: Emissivity of rough sea surface for 8-13 μm: modeling and verification. *Applied Optics*, **36,** 2609-2619

Xu, F., and A. Ignatov (2010), Evaluation of in situ SSTs for use in the calibration and validation of satellite retrievals, *J. Geoph. Res.*, **115**, *C09022*, doi:10.1029/21010JC006129.

Závody, A. M., C. T. Mutlow, and D. T. Llewellyn-Jones, 1995: A radiative transfer model for sea-surface temperature retrieval for the Along Track Scanning Radiometer. *J. Geophys. Res.*, **100,** 937-952